TET1-DNA Hydroxymethylation Mediated Oligodendrocyte Homeostasis is Required for CNS Myelination and Remyelination

Ming Zhang[1,7], Jian Wang[1,7], Kaixiang Zhang[1,7], Guozhen Lu[1], Keke Ren[1], Wenting Wang[1], Junlin Xing[1], Xingchun Gao[3], Weilin Jin[4], Honghui Mao [1], Lingli Xu[2], Kalen Berry[2], Hehuang Xie[5], Katsuhiko Mikoshiba[6], Shengxi Wu[1, *], Q. Richard Lu[2, *] and Xianghui Zhao[1, *]

[1] Department of Neurobiology, School of Basic Medicine, Fourth Medical University, Xi'an, Shaanxi 710032, China

[2] Division of Experimental Hematology and Cancer Biology, Brain Tumor Center, Cincinnati Children's Hospital Medical Center, Cincinnati, OH 45229, USA

[3] Shaanxi Key Laboratory of Brain Disorders, Xi'an, Shaanxi 710021, China

[4] School of Electronic, Information and Electrical Engineering, Shanghai Jiao Tong University, Shanghai 200240, China

[5] School of Neuroscience & Department of Biological Sciences, Virginia Tech, Blacksburg, VA 24061, USA

[6] Shanghai Institute for Advanced Immunochemical Studies, ShanghaiTech University, Shanghai 200031, China

[7] These authors contributed equally to this work.

*Corresponding authors

Shengxi Wu. Email: shengxi@fmmu.edu.cn

Q. Richard Lu. Email: richard.lu@cchmc.org

Xianghui Zhao. Email: xianghuizhao@fmmu.edu.cn

Abstract

Ten-eleven translocation (TET) proteins, encoding dioxygenase for DNA hydroxymethylation, are important players in nervous system development and diseases. However, their role in oligodendrocyte homeostasis, myelination and remyelination remains elusive. Here, we detected a genome-wide and locus-specific DNA hydroxymethylation landscape shift during oligodendrocyte-progenitor (OPC) differentiation. Ablation of *Tet1*, but not *Tet3*, results in stage-dependent defects in oligodendrocyte development and myelination in the brain. The mice lacking *Tet1* in the oligodendrocyte lineage develop schizophrenia-like behaviors. We further show that TET1 is also required for proper remyelination after demyelination injury in the adult mice. Transcriptomic and DNA hydroxymethylation profiling revealed a critical TET1-regulated epigenetic program for oligodendrocyte differentiation and identified a set of TET1-5hmC target genes associated with myelination, cell division, and calcium transport. *Tet1*-deficient OPCs exhibited reduced calcium activity in response to stimulus in culture. Moreover, deletion of a TET1-5hmC target gene, *Itpr2*, an oligodendrocyte-enriched intracellular calcium-release channel, significantly impaired the onset of oligodendrocyte differentiation. Together, our results suggest that stage-specific TET1-mediated epigenetic programming and oligodendrocyte homeostasis is required for proper myelination and repair.

Keywords: DNA hydroxymethylation, TET dioxygenases, epigenetics, oligodendrocyte, differentiation, calcium transport, type 2 IP_3 receptor

Introduction

Myelination by oligodendrocytes (OLs) enables saltatory conduction of action potentials and provides long-term trophic support for axons, maintaining integrity throughout the central nervous system (CNS) [1]. The formation of mature myelinating OLs is a complex process that is tightly coordinated spatially and temporally by genetic and epigenetic events [2, 3]. Epigenetic regulation by DNA methylation, histone modification, and chromatin remodeling is critical for multiple aspects of OL development, function, and regeneration [4-6]. For instance, proper maintenance of genomic 5-methyl cytosine (5mC) is essential for normal development, homeostasis, and function of mammalian cells [7, 8]. Genetic ablation of *Dnmt1*, which encodes the DNA methyltransferase that maintains DNA methylation after replication, results in impaired OL precursor cell (OPC) expansion and differentiation during early development [9].

The modified nucleotide 5-hydroxymethylcytosine (5hmC) has been shown to be an intermediate product generated during cytosine demethylation [10, 11]. DNA demethylation, like methylation, is a highly regulated process. DNA demethylation is mediated by the Ten-Eleven Translocation (TET) family of dioxygenases. The TET enzymes oxidize 5mC into 5hmC to initiate the DNA demethylation process [11, 12]. Dynamic regulation of cytosine methylation or demethylation has been established as common epigenetic modification regulating various processes from development to diseases in a cell-type and context-dependent manner [13-15]. TET enzymes are present in OL lineage cells [16], and here we interrogated how DNA demethylation contributes to OL lineage development, myelination, and remyelination after injury.

In this study, we demonstrate that there is a genome-wide shift in 5hmC landscape during OL specification and identify an age-dependent function of TET1 in OL lineage development and homeostasis. The mice with *Tet1* deletion in OL lineage develop schizophrenia-like behaviors. In addition, we show that TET1-regulated epigenetic program is required for efficient remyelination as depletion of *Tet1* in OPCs impairs myelin recovery after demyelinating injury in adult animals. Moreover, *Tet1* depletion resulted in genome-wide alterations in 5hmC and transcriptomic profiles that are associated with OPC differentiation and myelination, as well as calcium transport. Ablation of Itpr2, one of the TET1-5hmC targets that responsible for calcium release from endoplasmic reticulum in the OL lineage significantly impairs oligodendrocyte differentiation. These data suggest that TET1 and DNA hydroxymethylation mediated transcriptional and epigenetic programming regulate oligodendrocyte homeostasis and are required for proper myelination and animal behaviors.

Results

Dynamic DNA hydroxymethylation landscape during OL lineage differentiation

To investigate the 5hmC landscape during the OL lineage transition, we carried out antibody-

based 5hmC immunoprecipitation combined with Illumina sequencing (hMeDIP-seq) [17, 18] and analyzed 5hmC distribution across the genome. We compared the 5hmC distribution within OPCs to that in neural progenitor cells (NPCs) [19] and identified 1237 genes that were specifically hydroxymethylated in the promoter or transcription start site (TSS) regions of OPCs but not NPCs (Fig. 1a). Gene ontology analysis revealed that these genes involved in OPC differentiation are highly associated with terms such as cell projection organization, fatty acid transport, and regulation of cytosolic calcium ion concentration and with signaling pathways that are essential for OL development such as the G-protein coupled receptor pathway [20, 21] (Fig. 1b). Similarly, gene set enrichment analysis (GSEA) for 5hmC peaks in the gene body regions indicated that genes associated with bipotent progenitor, oligodendrocyte progenitor and postmitotic oligodendrocyte were enriched in OPCs (Fig. 1c), while pluripotent stem cell associated genes were enriched in NPCs (Fig. 1c). Comparison with a neural cell-type transcriptome dataset [22] (Supplementary Fig. 1) showed that the 5hmC signals were higher in OPCs than NPCs, in gene loci of OPC-associated genes, e.g. *Cspg4* (chondroitin sulfate proteoglycan 4) (Fig. 1d), immature OL-associated genes, e.g. *Tmem141* (transmembrane protein 141) (Fig. 1e) and mature OL-associated genes, e.g. *Mag* (myelin-associated glycoprotein) (Fig. 1f). In contrast, the genes with 5hmC peaks enriched in NPCs were associated with negative regulation of OL differentiation, such as *Id2 and Zfp28* (Fig. 1g). These data suggested a unique distribution pattern of genomic 5hmCs in the gene loci associated with OL lineage progression during the transition from NPCs to OPCs.

Deletion of *Tet1* in OL lineage causes myelination deficits at early postnatal stages

TET1-3 enzymes are present in OL lineage cells [16]. As TET2 had no detectable effects in OL lineage development [23], we assessed the functions of TET1 and TET3 in OL development. We crossed *Tet1*$^{f/f}$ mice [24] and *Tet3*$^{f/f}$ mice [18] with the *Olig1-Cre* line [25] to knockout the catalytic domains of these TET enzymes early in OL lineage development (Fig. 2a and Supplementary Fig. 2a). The resulting *Tet1*$^{flox/flox}$;*Olig1*Cre$^{+/-}$ (*Tet1* cKO) and *Tet3*$^{flox/flox}$;*Olig1*Cre$^{+/-}$ (*Tet3* cKO) mice were born at Mendelian ratios and appeared normal at birth. We did not detect significant differences in either the number of CC1^{+} mature OLs or myelin protein expression between heterozygous *Tet1* floxed mice (*Tet1*$^{flox/+}$;*Olig1*Cre$^{+/-}$), *Cre* control (*Tet1*$^{+/+}$;*Olig1*Cre$^{+/-}$), or wild-type mice (Supplementary Fig. 3a-b). Therefore, heterozygous littermates were used as controls. To assess Cre-mediated *Tet1* depletion, we quantified TET1 expression in OPCs from *Tet1* cKO and control mice at P4. Immunostaining revealed that expression of TET1 in the corpus callosum was significantly lower in *Tet1* cKO than control mice (Fig. 2b-c). TET1 levels were also decreased in purified OPCs from *Tet1* cKO mice than from control mice assayed by quantitative real-time PCR (Supplementary Fig. 3c).

To investigate the effects of TET1 on OL development in the brain, we examined the expression of Sox10 (an OL lineage marker) and mature OL markers CC1 and MBP. The number of $CC1^+$ mature OLs was significantly reduced in juvenile *Tet1* cKO mice compared to controls (Fig. 2d-e), but this difference was not observed in P60 adults (Fig. 2e, Supplementary Fig. 4a). Expression of MBP was also substantially decreased in both cortex (gray matter) and corpus callosum (white matter) in *Tet1* cKO mice compared to controls at P16 (Fig. 2f), but the levels were similar in adult animals (Supplementary Fig. 4a). These observations indicate that *Tet1* loss causes a delay in OL maturation. Similar experiments in the *Tet3* cKO animals did not show any significant differences between mutants and controls (Supplementary Fig. 2). Therefore, we focused on examining the processes underlying the observed myelination defects in *Tet1* cKO mice.

In addition, electron microscopy (EM) revealed that the number of myelinated axons was significantly reduced in *Tet1* mutants compared to controls at both P14 optic nerves and P27 corpus callosum (Fig. 2g-h, j). Moreover, those myelinated axons in *Tet1* cKO mice were characterized by higher G ratios and thinner myelin sheaths than those of control mice (Fig. 2i, k). However, the myelin ultrastructure defects were not observed in P60 adult *Tet1* cKO animals (Supplementary Fig. 4b-d). Together, these results suggest a stage-dependent function of TET1 in CNS myelination.

To evaluate the neurological significance of hypomyelination in *Tet1* cKO mice, we analyzed stimulus-evoked compound action potential (CAP) in optic nerves as previously described [26, 27]. Suction electrodes back filled with artificial cerebrospinal fluid were used for stimulation and recording. In *Tet1* mutants, both the peak amplitudes and the CAP areas, which are indexes of excited myelinated axon numbers and nerve function [26, 27], were significantly lower than controls under all stimulating currents tested (Fig. 2l-n). This observation indicates that hypomyelination impairs action potential transduction in *Tet1* cKO mice.

Loss of TET1 function in OLs induces schizophrenia relevant behaviors in the animal

Multiple studies have associate TET-5hmC with psychiatric and cognitive disorders [28-30], and multivariable logistic regression showed that ErbB4, BDNF and TET1 were independent predictors for schizophrenia [31]. To gain insight into the physiological function of TET1 in animal behaviors, *Tet1* cKO mice were subjected to behavior tests relevant to schizophrenia. *Tet1* cKO mice did not exhibit differences in weight and whisker number in comparison with control littermates.

First, we investigated the performance of juvenile *Tet1* mutant in Prepulse Inhibition (PPI) of startle, which is a common test of sensorimotor gating ability for schizophrenia patients [32]. Reduced PPI ability due to an exaggerated acoustic startle reflex (ASR) is thought to contribute

to schizophrenic conditions. We found that the input/output function and the startle response were comparable between control and *Tet1* mutant mice (Supplementary Fig. 5a), indicating the normal hearing and motor abilities (i/o function) in *Tet1* cKO mice. However, when using a combination of auditory-evoked startle (120dB) and three levels of prepulse (70, 76 and 82 dB) to compare ARS, we observed that PPI was significantly attenuated in *Tet1* cKO mice in comparison with control animals (Supplementary Fig. 5b), suggesting the impaired sensorimotor gating ability in *Tet1* mutant.

Since working memory deficits are characteristic features in schizophrenia, *Tet1* cKO mice and control littermates were evaluated for their performance in Morris water maze to assess their working memory. Five-day acquisition trials exhibited similar swim paths, swim velocity and escape latency to the platform between control and *Tet1* cKO groups (Supplementary Fig. 5c-e), which indicates that *Tet1* mutants had normal swimming and learning abilities. However, in the sixth-day probe trial, the escape latency was significantly higher in *Tet1* cKO mice than in control mice (Supplementary Fig. 5f), and the number of crossing the position was greatly reduced in mutant mice (Supplementary Fig. 5g). Additionally, in contrast to controls, the *Tet1*cKO mice showed no preference for the target quadrant over other three quadrants, (Supplementary Fig. 5h-i). These observations suggest that *Tet1* cKO mice exhibit impaired PPI and working memory, resulting in schizophrenia-like behaviors.

Ablation of *Tet1* results in defects in OPC cell-cycle progression

Concomitant with the myelin deficiency, we observed a marked reduction of Olig2$^+$ cells from embryonic stage E15.5 and at P1 in *Tet1* cKO cortex relative to controls (Fig. 3a-b). Moreover, the number of PDGFRα$^+$ cells in the mutant cortex was significantly reduced at E15.5 and P1 (Fig. 3a, c), suggesting a downsized OPC pool.

To determine the underlying defects that led to the observed reduction in the OPC and OL population in juvenile *Tet1* mutants, we first tested the possibility that OPCs are more likely to undergo apoptosis in the mutant with the TUNEL assay. Brain sections from E14.5, E17.5 and P1 mice revealed no distinguishable changes in the number of apoptotic cells among Olig2$^+$ OL lineage cells between *Tet1* cKO animals and control littermates (Supplementary Fig. 6a-b).

Next, we performed BrdU incorporation assay to examine the proliferation of OPCs. At P1, mice were dosed with BrdU and sacrificed 2 hours later. Compared to controls, intriguingly, the percentage of BrdU$^+$ cells in Olig2$^+$ OL lineage cells showed a significant increase in *Tet1* cKO cortex (Fig. 3d-e). The reduction of OPC numbers in *Tet1* cKO mice thus promote us to investigate if there is a cell-cycle defect in *Tet1*-deficient OPCs. We performed flow cytometry for purified OPCs in which DNA was stained with propidium iodide. Significant increases in the percentages of cells in S phase (23.4 ± 0.85%) and G2/M phase (13.39 ± 1.01%) were observed

in OPCs from *Tet1* mutants compared to the controls (9.02 ± 0.99% for S phase and 8.29 ± 0.62% for G2/M phase) (Fig. 3f-g). Moreover, there was a concomitant reduction in the number of cells in G1 phase in *Tet1* mutants compared to the controls (Fig. 3f-g). These results suggest that the proliferation of OPCs from *Tet1* cKO brains is blocked at the transition from G2/M to G1 phase, which likely leads to the observed reduction in OPC numbers in *Tet1* cKO mice.

To determine if defects in OL differentiation caused by TET1 deletion are cell-autonomous, we isolated primary OPCs from the neonatal cortices of control and *Tet1* cKO pups, and then treated them with T3 to promote differentiation. Immunostaining results showed that the number of CNP^+ cells and MBP^+ cells in *Tet1* deficient OPCs were significantly decreased when compared with control OPCs at Day 3 and Day 5 (Fig. 3h-i), suggesting that *Tet1*-depleted OPCs are intrinsically reduced in their differentiation capacity.

In addition, we noted that *Tet1* deletion did not substantially alter the number of other neural cell types in the brain. Western blot and immunostaining with antibodies against DCX, a marker for newly generated neurons; NeuN, a mature neuron marker; and ALDHL1, an astrocyte marker, revealed comparable neuron and astrocyte pools between controls and *Tet1* mutants (Supplementary Fig. 6c-g). Taken together, our data suggest that the abnormal cell-cycle progression of OPCs and delayed OPC differentiation contribute to the reduced OL numbers and hypomyelination in juvenile *Tet1*-deficient mice.

TET1 regulates the transition from OPCs to OLs

Since the impaired myelination in *Tet1* cKO mice may result from the downsized OPC pool, to further confirm the role of TET1 in OL differentiation after birth, we bred *Tet1*$^{flox/flox}$ mice with *NG2-CreER*^{T} line [33], an OPC-specific tamoxifen-inducible Cre line to generate *NG2-CreER*^{T}:*Tet1*$^{flox/flox}$ (*Tet1* OPC-iKO) animals. The *Tet1* OPC-iKO mice were treated daily with tamoxifen from P2 through P5 to induce *Tet1* deletion (Fig. 4a) and double immunostaining confirmed TET1 loss in $Sox10^+$ cells (Fig. 4b-c). Heterozygous littermates (*NG2-CreER*^{T}:*Tet1*$^{flox/+}$) were served as controls. In P7 corpus callosum, more $PDGFR\alpha^+/Ki67^+$ cells and less MBP^+ cells were observed in *Tet1* OPC-iKO mice (Fig. 4d-g). Moreover, a reduction in $CC1^+$ OLs and MBP intensity was observed in corpus callosum from P14 *Tet1* OPC-iKO mice (Fig. 4h-i). These results indicate that TET1 is required for the transition from OPCs to OLs.

Efficient remyelination requires TET1 function

Given the critical role of TET1 in early oligodendrocyte development, we reasoned that TET1 should also be required in the adult brain for remyelination after injury that results in demyelination. We induced demyelinated lesions in the corpus callosum via stereotaxic guided lysolecithin (LPC) injections (Fig. 5a). LPC induces rapid myelin breakdown followed by myelin

regeneration through an OPC recruitment phase at 7 days post-lesion (7 dpl) induction and a remyelination phase at 14 dpl. TET1$^+$ cell numbers were increased substantially in the lesion site at 7 dpl relative to controls injected with vehicle (Fig. 5b-c). In particular, the expression levels of TET1 in Olig2$^+$ cells were higher after LPC treatment (Fig. 5b-c).

To evaluate the role of TET1 in remyelination, we used *NG2-CreER*^{T}:*Tet1*$^{flox/flox}$ (*Tet1* OPC-iKO) animals mentioned above. To induce recombination in adult mice, 8-week-old *Tet1* OPC-iKO mice were injected daily with tamoxifen for 8 days, starting 3 days prior to LPC injection in the corpus callosum (Fig. 5d). Brains were harvested at 7, 14 and 21 dpl from *Tet1* OPC-iKO mice and heterozygous controls. To determine the extent of remyelination, we examined the expression of OPC markers and myelin-related genes. Loss of *Tet1* did not appear to impair the recruitment of PDGFRα$^+$ OPCs, and the numbers of OPCs in the lesions were comparable between control and *Tet1* OPC-iKO mice during the recruitment phase at dpl 7 (Fig. 5e, f). In contrast, there were significantly fewer GST-pi$^+$ differentiating OLs in the lesion site during the remyelination phase at dpl 14 and dpl 21 in *Tet1* OPC-iKO mice relative to controls (Fig. 5e, g). Consistent with a reduction in the number of differentiating OLs, MBP was also reduced in *Tet1*-iKO lesions compared to those of controls at dpl 21 (Fig. 5h). Notably, far fewer remyelinated axons were detected in the lesions of *Tet1*-iKO mice than controls at dpl 28 (Fig. 5i-j). Furthermore, the thicknesses of newly generated myelin sheaths around axons were significantly reduced in *Tet1*-iKO mutants (Fig. 5k). These observations indicate that TET1 is required for the proper remyelination in the context of white matter injury.

Transcriptome alterations and a genome-wide decrease of 5hmC in *Tet1*-ablated OPCs

To investigate the molecular underpinnings of the observed defects in early oligodendrocyte development, we compared the RNA transcriptomes of OPCs cultured from control and *Tet1* cKO neonates. There were approximately 1880 genes downregulated and 881 genes upregulated in *Tet1* mutants compared with controls (FDR<0.05, Log_2>1 or <-1) (Supplementary Table 1), suggesting that the predominant effect of *Tet1* loss was transcriptional repression. As indicated by gene set enrichment analysis (GSEA), among the top downregulated TET1 targets were those pertinent to cell division, extracellular matrix and oligodendrocyte differentiation (Fig. 6a-d), which are in consistent with the abnormal cell cycle and deficient myelin formation in *Tet1* mutants. In contrast, gene ontology terms associated with the mitochondria gene module and immune-related functions were upregulated in *Tet1* cKO OPCs (Fig. 6a-b, e-f). Quantitative PCR confirmed representative gene expression changes associated with these gene set enrichments in the RNA-seq data (Fig. 6g-i). Specifically, OL differentiation and myelination-associated genes *Mbp*, *Plp1*, *Myrf*, *Enpp2*, *Cnp*, *Cldn11*, *Ugt8a*, *Kif11*, and *Bcas1* were markedly downregulated in *Tet1* deficient OPCs (Fig. 6g) as were genes involved in cell-cycle regulation (Fig. 6h). The

transcriptome landscape alterations in *Tet1* cKO OPCs were in line with the observations that *Tet1* depletion led to cell-cycle progression defects and hypomyelination phenotypes.

Since TET1 mediates DNA hydroxymethylation/demethylation, we next tested the level of 5hmC in oligodendrocytes from *Tet1* mutants. In P27 brain sections, immunostaining of 5hmC simultaneously with the OL marker CC1 revealed a striking reduction in 5hmC intensity in oligodendrocytes (Fig. 7a-b), which strongly suggested that 5hmC is involved in TET1-mediated regulation of OL differentiation. To further compare the genome-wide 5hmC distributions, we performed hMeDIP-seq in OPC cultures from controls and *Tet1* mutants. *Tet1* cKO OPCs showed a dramatic reduction in 5hmC peak signals compared to controls (Supplementary Fig. 7a). In both groups, most 5hmC peaks resided in intergenic regions; less than 40% of peaks were within gene bodies of annotated RefSeq genes (Supplementary Fig. 7b). This is different from the distribution pattern in mouse embryonic stem cells [18] and neurons [34]. After plotting the distribution of 5hmC peaks over RefSeq genes, we found that 5hmC was reduced near the transcription start sites (TSSs) and transcription terminal sites (TTSs) in control OPCs and that *Tet1* depletion caused reductions of 5hmC, especially in intragenic regions, promoter regions, and TTS regions (Fig. 7c and Supplementary Fig. 7b). Heatmap clustering of the 5hmC peak distributions 5-kb upstream and downstream of TSSs revealed five groups; levels of 5hmC signals were lower in all five groups in *Tet1* cKO samples than in the control samples (Fig. 7d). Further analysis showed that most differentially hydroxymethylated regions also had low CpG density of less than 1 CpG per 100 bp (Supplementary Fig. 7c).

We next examined the effects of hydroxymethylation on gene expression. By integrating RNA-seq data with hMeDIP-seq data, we observed that among the genes that had lower hydroxymethylation in gene body regions in the *Tet1* cKO mice than in controls, 12.83% had expression downregulated (1026 of 7998) and 4.89% had expression upregulated (391 of 7998) (Supplementary Fig. 7d). The percentages were comparable in promoter regions that were differentially hydroxymethylated with 13.46% of genes downregulated and 6.42% upregulated genes (Supplementary Fig. 7e). These observations indicate that DNA hydroxymethylation is positively correlated with gene expression.

Among the genes that showed both downregulated mRNA expression and decreased gene body 5hmC levels in *Tet1* cKO mice, gene ontology analysis revealed that a majority of them are associated with oligodendrocyte differentiation, cell proliferation and extracellular matrix (Fig. 7e-f). For example, *Mbp*, *Mobp*, and *Cnp* are myelin-related genes; *Tcf7L2*, *Myrf*, and *Enpp2/6* are involved in the regulation of OL differentiation in a stage-specific manner within different transcriptional circuitries [35, 36]. Snapshots of 5hmC profiles of representative myelination genes and cell division genes showed reduced 5hmC levels in *Tet1* cKO group (Fig. 7g and Supplementary Fig. 7f). Together, these results are highly in consistent with the hypomyelination

phenotypes in *Tet1* cKO mice and indicate the significance of TET1-5hmC mechanisms in OL homeostasis.

Impaired calcium transport leads to differentiation defects in OPC cultures from *Tet1* cKO mice

When searching for TET1-5hmC regulated factors that may involve in OL development and homeostasis, we noticed that there was a cluster of calcium transporter genes among the downregulated and hypohydroxymethylated genes in *Tet1* cKO group (Fig.6a-b and Fig. 7e-f, h-i). The decrease in expression of these genes in *Tet1* cKO mice was confirmed by qRT-PCR assays (Fig. 7j). CACNA1a, CACNA1c, CACNA2d1, CACNB4, and CACNG5 are plasma membrane voltage-operated Ca^{2+} channels (VOCCs) that are expressed in OPCs and contribute to calcium dynamics in these cells [22, 37]. In particular, calcium influx mediated by CACNA1c, also known as $Ca_v1.2$, is required for oligodendrocyte differentiation [38, 39]. Another target gene *Itpr2*, which encodes a type 2 IP_3 receptor, localized to the endoplasmic reticulum (ER) and expressed exclusively in postmitotic OLs [40, 41], also had decreased mRNA expression in OPCs from *Tet1* cKO mice compared to controls (Fig. 7j). These data indicate that TET1-5hmC targets calcium transport genes and may regulate calcium dynamics in oligodendrocytes.

To evaluate the intracellular Ca^{2+} concentration ($[Ca^{2+}]_i$) fluctuation in OPC culture, a Fluo4-based Ca^{2+}-imaging approach was employed. ATP can mobilize Ca^{2+} from ER stores or trigger Ca^{2+} influx across the plasma membrane [42, 43]. To first determine the intracellular calcium release, we used calcium free aCSF to load Fluo-4. In OPC cultures, application of ATP induced a transient increase of $[Ca^{2+}]_i$ in both control and *Tet1* cKO groups (Fig. 8a-b, Supplementary Movie 1 and 2). The amplitude of ATP-induced calcium rise was significantly higher in control OPCs than in *Tet1* mutant OPCs (Fig. 8c), and the kinetics of onset were slower in mutant OPCs as well (Fig. 8d). These results indicate a deficit of intracellular calcium mobilization in *Tet1* depleted OPCs. To further examine the extracellular calcium influx in *Tet1* cKO OPCs, we used Bay K 8644, a L-type calcium channel (L-VOCC) agonist [44], to induce synchronous calcium transient in OPCs, which can be blocked by the specific L-VOCC inhibitor verapamil (Supplementary Fig. 8a). In the mutant OPCs, $[Ca^{2+}]_i$ increase was of lower amplitude and the kinetics of onset were slower (Supplementary Fig. 8b-c), suggesting the attenuated function of membrane calcium channel in *Tet1* ablated OPCs.

To investigate the consequences of impaired calcium rise in *Tet1*-deficient OPCs, we examined cell differentiation after activating calcium signaling. Consistent with the results of high K^+ application [39], three consecutive pulses (5 min/each) daily with 10 μM calcium channel agonist Bay K 8644 significantly promoted differentiation of OPCs and restored the differentiation defects in *Tet1* deficient OPCs as determined by qRT-PCR analysis of myelin genes and MBP^+ OL

formation (Supplementary Fig. 8d-f). These data indicate that TET1-modulated $[Ca^{2+}]_i$ rise play important roles in the OL differentiation process.

Ablation Itpr2, modulator for calcium release from endoplasmic reticulum, inhibits OL differentiation

To further distinguish calcium signaling as TET1-5hmC target during OL differentiation, or the results of impaired differentiation in *Tet1* cKO mice, we then tested the function of Itpr2, one of TET1-5hmC target calcium transport genes, in myelination. As modulator for calcium release from ER, Itpr2 showed highest expression in postmitotic newly formed oligodendrocytes (OL-1DIV, PDGFRα$^-$/CNPase$^+$) (Fig.8e) as reported previously [40, 41]. In *vitro* studies with RNAi methods revealed that transfection of siRNA against Itpr2 in normal OL cultures significantly reduced the expression of myelin genes and impairs OL differentiation (Fig. 8f-h, Supplementary Fig.8g-h).

Investigation with *Itpr2* conditional knockout mice also confirmed the function of Itpr2 in OL development. *Itpr2*$^{flox/flox}$;*Olig1*Cre$^{+/-}$ (*Itpr2* cKO) mice were born at Mendelian ratios and appeared normal at birth. To assess Cre-mediated *Itpr2* depletion, we quantified Itpr2 expression in Olig2$^+$ cells from *Itpr2* cKO and control mice at P14. Immunostaining revealed that expression of Itpr2 in the corpus callosum was significantly lower in *Itpr2* cKO than in control mice (Fig. 8i-j). Examination the expression of stage specific OL lineage markers, PDGFRα and CC1, revealed that more PDGFRα$^+$ OPCs were observed in P7 and P14 *Itpr2* mutant brain (Fig. 8k-l); however, the percentage of CC1$^+$ mature OLs among Olig2$^+$ cells was significantly reduced in *Itpr2* cKO mice compared to controls during development (Fig. 8k, m). Myelin protein expression was also substantially decreased in *Itpr2* cKO mice compared to controls at P31 (Fig. 8n). Electron microscopy of P16 optic nerves revealed that the number of myelinated axons was significantly reduced in *Itpr2* mutants (Fig. 8o-p), and the G ratio was higher in mutant (Fig. 8q). These results suggest that as one of the target genes of TET1-5hmC, Itpr2 accumulates after cell cycle withdrawal and is involved in the initiation of oligodendrocytes differentiation, probably by effectively releasing calcium from ER.

Discussion

TET1 functions stage-specifically in OL development and remyelination

Methylation of cytosine on CpG islands in the genome enables stable but reversible transcription repression and is critical for mammalian development [7, 8]. Defects in the regulation of DNA methylation are associated with various neurological diseases [45, 46]. TET enzymes catalyze the first step of DNA demethylation by oxidizing 5mC into 5hmC [10-12]. Strikingly, we detected a genome-wide change in the DNA demethylation landscape marked by 5hmC during OPC

differentiation from neural progenitor cells, suggesting a role of TET-mediated DNA demethylation in regulation of OL lineage progression.

We found that TET1, but not TET3, is critical for OPC proliferation, differentiation, and myelination during early animal development, suggesting a unique function of TET1 in oligodendrogenesis and subsequent myelinogenesis. Despite early developmental defects, we noticed that the developmental myelin deficiencies recovered in adult *Tet1* cKO mice, which might be due to the expansion of OL numbers that escaped from Cre-mediated *Tet1* depletion. The remyelination capacity after injury was compromised in adult *Tet1* OPC-iKO brains, suggesting that TET1 is also critical for the myelin regeneration process.

Although OL differentiation defects were not due to increased apoptosis in the *Tet1* cKO mutant brain, we found that OPC cell cycle progression was impaired in the developing brain of *Tet1* cKO animals. TET1 has been implicated in regulation of cell-cycle progression. For instance, TET1 is critical to the stability of cyclin B1 and acts as a facilitator of mitotic cell-cycle progression [47, 48]. In line with these studies, we showed that *Ccng2*, *Cdca3, Ccna2*, *Ccnb2*, and *Cdc25b*, which encode factors involved in cell-cycle regulation [49-53] were 5hmC enriched genes in OPCs and were down-regulated in *Tet1* cKO OPCs, suggesting that TET1 is also critical for cell-cycle progression in OPCs.

TET1-5hmC functions in psychological disorders

TET-5hmC association with psychiatric and cognitive disorders has gained increasing recognition in recent years [28-30]. A cohort of new autosomal recessive genes for intellectual disability, including the missense mutations in TET1, has been identified [54]. TET1 together with other factors such as ErbB4, BDNF was identified as independent predictors of schizophrenia, and serves a high risk gene for schizophrenia [31]. We find that mice with *Tet1* cKO in the oligodendrocyte lineage exhibit impaired PPI and working memory deficits, the key behavior phenotypes related to schizophrenia. Thus, our studies demonstrate a crucial function of TET1-mediated epigenetic modifications in oligodendrocytes for schizophrenia and related brain disorders.

Locus-specific alterations of DNA hydroxymethylation in OPCs of *Tet1* mutants

Levels of 5hmC are variable in the promoter and gene body regions [55] and impact gene expression in a cell type-dependent manner [18, 56, 57]. Our comparison of differentially hydroxymethylated genes with transcriptome profiles indicated that 5hmC signals in gene bodies are more significantly associated with gene expression changes than those in promoter regions in OPCs. This suggests that 5hmC modification by TET1 regulates locus-specific gene expression programs necessary for OPC differentiation. 5hmC may regulate gene expression through associations with various regulatory elements [15, 58], including histone modification and

chromatin configuration. For example, in ESCs, 5hmC accumulates in “bivalent domains” in promoters or enhancers that are decorated with both activating (H3K4me3) and repressing (H3K27me3) histone marks [59, 60]. How 5hmCs cooperate with other epigenetic regulators for OPC differentiation remains to be determined.

Intriguingly, ablation of *Tet1* led to upregulation of a set of genes in OPCs, indicating that TET1-mediated 5hmC deposition may also function as a transcriptional repressor. Consistent with our data, inhibition of *Tet1* expression increased expression of a set of genes in ESCs [61, 62]. TET1-mediated repression might involve recruitment of the MBD3/NuRD repressor complex, which was shown to co-localize with TET1 in ESCs [63]. TET1 may also coordinate with Sin3A co-repressor complex, which has a similar binding profile to TET1 and is required for a subset of TET1-repressed target genes [61, 64]. A recent study indicates that TET1-mediated transcriptional repression could channel through JMJD8 demethylase transcriptional repressor and is independent of TET1 catalytic activity during epiblast differentiation [65]. The mechanisms of locus-specific transcriptional regulation by TET1 during OL development remain to be further defined.

TET1-5hmC regulates calcium transport to control proper oligodendrocyte differentiation

Calcium signaling is important for OPC migration, differentiation, and initiation of myelin formation [66-69]. For instance, blocking of voltage-gated Ca^{2+} entry in OPCs inhibits their maturation and myelin formation ability [39]. Similarly, an increase of the resting $[Ca^{2+}]_i$ through membrane depolarization facilitates MBP synthesis in OPCs [67]. We found that *Tet1* deletion led to the downregulation of multiple calcium transporter genes in OPCs, which mediated the impaired intracellular store release and extracellular influx in response to stimulus. Moreover, treatment with a calcium channel agonist reversed the differentiation defects in *Tet1*-deficient OPCs, thus indicating the significance of TET1-5hmC regulated calcium transport in OLs.

We find that Itpr2, an intracellular calcium channel that exclusively expressed in postmitotic OLs [40, 41], is one of TET1-5hmC targets. Expression of Itpr2 is upregulated during a motor learning task [41], indicating the participation of $Itpr2^+$ OLs in myelin plasticity. We find that deletion of *Itpr2* in the OL lineage greatly reduces OPC differentiation, suggesting that Itpr2 is critical for an initiation for myelination. Thus, TET1 mediated 5hmC modification, or DNA hydroxymethylation, can modulate the process of oligogenesis and myelinogenesis through at least two critical processes, by fine-tuning cell cycle progression for OPC proliferation and by regulating oligodendrocyte hemostasis e.g., Itpr2-mediated calcium transport, for OL myelination.

Acknowledgements

The authors would like to thank Dr. Fangfang Liu, Dr. Bo Zhao, Dr. Feng Zhang, Junjun Kang, and Haifeng Zhang for great technical support; Dr. Natalie Lai Man Wu for GSEA analysis; Dr.

Weidong Tian, Dr. Feng Zhang, Dr. Yazhou Wang, Dr. Ceng Lou, Dr. Jinxiang Dai, and Dr. Yaqi Deng for helpful suggestions; and Dr. Guoliang Xu for *Tet1*^{loxp} lines. This work was funded by grants from National Natural Science Foundation of China (Grant number: 31571050 and 313710757).

References:

1. Nave, K.A. & Werner, H.B. Myelination of the nervous system: mechanisms and functions. *Annu Rev Cell Dev Biol* **30**, 503-533 (2014).
2. Emery, B. & Lu, Q.R. Transcriptional and Epigenetic Regulation of Oligodendrocyte Development and Myelination in the Central Nervous System. *Cold Spring Harbor perspectives in biology* **7**, a020461 (2015).
3. Zuchero, J.B. & Barres, B.A. Intrinsic and extrinsic control of oligodendrocyte development. *Current opinion in neurobiology* **23**, 914-920 (2013).
4. Gregath, A. & Lu, Q.R. Epigenetic modifications-insight into oligodendrocyte lineage progression, regeneration, and disease. *FEBS letters* **592**, 1063-1078 (2018).
5. Liu, J., Moyon, S., Hernandez, M. & Casaccia, P. Epigenetic control of oligodendrocyte development: adding new players to old keepers. *Current opinion in neurobiology* **39**, 133-138 (2016).
6. Lu, G.*, et al.* Epigenetic regulation of myelination in health and disease. *The European journal of neuroscience* **49**, 1371-1387 (2019).
7. Iurlaro, M., von Meyenn, F. & Reik, W. DNA methylation homeostasis in human and mouse development. *Current opinion in genetics & development* **43**, 101-109 (2017).
8. Smith, Z.D. & Meissner, A. DNA methylation: roles in mammalian development. *Nat Rev Genet* **14**, 204-220 (2013).
9. Moyon, S.*, et al.* Functional Characterization of DNA Methylation in the Oligodendrocyte Lineage. *Cell reports* (2016).
10. Kriaucionis, S. & Heintz, N. The nuclear DNA base 5-hydroxymethylcytosine is present in Purkinje neurons and the brain. *Science* **324**, 929-930 (2009).
11. Tahiliani, M.*, et al.* Conversion of 5-methylcytosine to 5-hydroxymethylcytosine in mammalian DNA by MLL partner TET1. *Science* **324**, 930-935 (2009).
12. Ito, S.*, et al.* Role of Tet proteins in 5mC to 5hmC conversion, ES-cell self-renewal and inner cell mass specification. *Nature* **466**, 1129-1133 (2010).
13. Graff, J., Kim, D., Dobbin, M.M. & Tsai, L.H. Epigenetic regulation of gene expression in physiological and pathological brain processes. *Physiological reviews* **91**, 603-649 (2011).
14. Sun, W., Zang, L., Shu, Q. & Li, X. From development to diseases: the role of 5hmC in brain. *Genomics* **104**, 347-351 (2014).
15. Szulwach, K.E.*, et al.* 5-hmC-mediated epigenetic dynamics during postnatal neurodevelopment and aging. *Nature neuroscience* **14**, 1607-1616 (2011).
16. Zhao, X.*, et al.* Dynamics of ten-eleven translocation hydroxylase family proteins and 5-hydroxymethylcytosine in oligodendrocyte differentiation. *Glia* **62**, 914-926 (2014).
17. Ficz, G.*, et al.* Dynamic regulation of 5-hydroxymethylcytosine in mouse ES cells and during differentiation. *Nature* **473**, 398-U589 (2011).
18. Gu, T.P.*, et al.* The role of Tet3 DNA dioxygenase in epigenetic reprogramming by oocytes. *Nature* **477**, 606-610 (2011).
19. Li, X.*, et al.* Ten-eleven translocation 2 interacts with forkhead box O3 and regulates adult neurogenesis. *Nature communications* **8**, 15903 (2017).
20. Chen, Y.*, et al.* The oligodendrocyte-specific G protein-coupled receptor GPR17 is a cell-intrinsic timer of myelination. *Nature neuroscience* **12**, 1398-1406 (2009).
21. Mogha, A., D'Rozario, M. & Monk, K.R. G Protein-Coupled Receptors in Myelinating Glia. *Trends Pharmacol Sci* **37**, 977-987 (2016).
22. Zhang, Y.*, et al.* An RNA-sequencing transcriptome and splicing database of glia, neurons, and vascular cells of the cerebral cortex. *The Journal of neuroscience : the official journal of the Society for Neuroscience* **34**, 11929-11947 (2014).
23. Moyon;, S.*, et al.* TET1-mediated DNA hydroxy-methylation regulates adult remyelination. *bioRxiv* (2019).
24. Zhang, R.R.*, et al.* Tet1 regulates adult hippocampal neurogenesis and cognition. *Cell stem cell* **13**, 237-245 (2013).
25. Xin, M.*, et al.* Myelinogenesis and axonal recognition by oligodendrocytes in brain are

uncoupled in Olig1-null mice. *The Journal of neuroscience : the official journal of the Society for Neuroscience* **25**, 1354-1365 (2005).
26. Devaux, J., Gola, M., Jacquet, G. & Crest, M. Effects of K+ channel blockers on developing rat myelinated CNS axons: identification of four types of K+ channels. *J Neurophysiol* **87**, 1376-1385 (2002).
27. Devaux, J. & Gow, A. Tight junctions potentiate the insulative properties of small CNS myelinated axons. *J Cell Biol* **183**, 909-921 (2008).
28. Rustad, S.R., Papale, L.A. & Alisch, R.S. DNA Methylation and Hydroxymethylation and Behavior. *Current topics in behavioral neurosciences* **42**, 51-82 (2019).
29. Madrid, A., Papale, L.A. & Alisch, R.S. New hope: the emerging role of 5-hydroxymethylcytosine in mental health and disease. *Epigenomics* **8**, 981-991 (2016).
30. Antunes, C., Sousa, N., Pinto, L. & Marques, C.J. TET enzymes in neurophysiology and brain function. *Neuroscience and biobehavioral reviews* **102**, 337-344 (2019).
31. Li, C.*, et al.* Assessment of a combination of Serum Proteins as potential biomarkers to clinically predict Schizophrenia. *International journal of medical sciences* **15**, 900-906 (2018).
32. Mena, A.*, et al.* Reduced Prepulse Inhibition as a Biomarker of Schizophrenia. *Frontiers in behavioral neuroscience* **10**, 202 (2016).
33. Zhu, X.*, et al.* Age-dependent fate and lineage restriction of single NG2 cells. *Development* **138**, 745-753 (2011).
34. Hahn, M.A.*, et al.* Dynamics of 5-hydroxymethylcytosine and chromatin marks in Mammalian neurogenesis. *Cell reports* **3**, 291-300 (2013).
35. Hornig, J.*, et al.* The transcription factors Sox10 and Myrf define an essential regulatory network module in differentiating oligodendrocytes. *PLoS genetics* **9**, e1003907 (2013).
36. Morita, J.*, et al.* Structure and biological function of ENPP6, a choline-specific glycerophosphodiester-phosphodiesterase. *Scientific reports* **6**, 20995 (2016).
37. Larson, V.A., Zhang, Y. & Bergles, D.E. Electrophysiological properties of NG2(+) cells: Matching physiological studies with gene expression profiles. *Brain Res* **1638**, 138-160 (2016).
38. Cheli, V.T.*, et al.* Conditional Deletion of the L-Type Calcium Channel Cav1.2 in Oligodendrocyte Progenitor Cells Affects Postnatal Myelination in Mice. *The Journal of neuroscience : the official journal of the Society for Neuroscience* **36**, 10853-10869 (2016).
39. Cheli, V.T., Santiago Gonzalez, D.A., Spreuer, V. & Paez, P.M. Voltage-gated Ca2+ entry promotes oligodendrocyte progenitor cell maturation and myelination in vitro. *Experimental neurology* **265**, 69-83 (2015).
40. Zeisel, A.*, et al.* Brain structure. Cell types in the mouse cortex and hippocampus revealed by single-cell RNA-seq. *Science* **347**, 1138-1142 (2015).
41. Marques, S.*, et al.* Oligodendrocyte heterogeneity in the mouse juvenile and adult central nervous system. *Science* **352**, 1326-1329 (2016).
42. Kirischuk, S., Scherer, J., Kettenmann, H. & Verkhratsky, A. Activation of P2-purinoreceptors triggered Ca2+ release from InsP3-sensitive internal stores in mammalian oligodendrocytes. *J Physiol* **483 (Pt 1)**, 41-57 (1995).
43. Stevens, B., Porta, S., Haak, L.L., Gallo, V. & Fields, R.D. Adenosine: a neuron-glial transmitter promoting myelination in the CNS in response to action potentials. *Neuron* **36**, 855-868 (2002).
44. Greenberg, D.A., Cooper, E.C. & Carpenter, C.L. Calcium channel 'agonist' BAY K 8644 inhibits calcium antagonist binding to brain and PC12 cell membranes. *Brain Res* **305**, 365-368 (1984).
45. Gopalakrishnan, S., Van Emburgh, B.O. & Robertson, K.D. DNA methylation in development and human disease. *Mutation research* **647**, 30-38 (2008).
46. Lu, H., Liu, X., Deng, Y. & Qing, H. DNA methylation, a hand behind neurodegenerative diseases. *Front Aging Neurosci* **5**, 85 (2013).
47. Chrysanthou, S.*, et al.* A Critical Role of TET1/2 Proteins in Cell-Cycle Progression of Trophoblast Stem Cells. *Stem cell reports* (2018).
48. Huang, S.*, et al.* Tet1 is required for Rb phosphorylation during G1/S phase transition. *Biochemical and biophysical research communications* **434**, 241-244 (2013).

49. Bennin, D.A., *et al.* Cyclin G2 associates with protein phosphatase 2A catalytic and regulatory B' subunits in active complexes and induces nuclear aberrations and a G1/S phase cell cycle arrest. *The Journal of biological chemistry* **277**, 27449-27467 (2002).
50. Boutros, R., *et al.* CDC25B overexpression stabilises centrin 2 and promotes the formation of excess centriolar foci. *PLoS One* **8**, e67822 (2013).
51. Kalaszczynska, I., *et al.* Cyclin A is redundant in fibroblasts but essential in hematopoietic and embryonic stem cells. *Cell* **138**, 352-365 (2009).
52. Nagi Ayad, S.R., Monica Murakami, Judith Jebanathirajah,Steven Gygi,and Marc W. Kirschner. Tome-1, a Trigger of Mitotic Entry, Is Degraded during G1 via the APC. *Cell* (2003).
53. Timofeev, O., Cizmecioglu, O., Settele, F., Kempf, T. & Hoffmann, I. Cdc25 phosphatases are required for timely assembly of CDK1-cyclin B at the G2/M transition. *The Journal of biological chemistry* **285**, 16978-16990 (2010).
54. Harripaul, R., *et al.* Mapping autosomal recessive intellectual disability: combined microarray and exome sequencing identifies 26 novel candidate genes in 192 consanguineous families. *Molecular psychiatry* **23**, 973-984 (2018).
55. Shi, D.Q., Ali, I., Tang, J. & Yang, W.C. New Insights into 5hmC DNA Modification: Generation, Distribution and Function. *Frontiers in genetics* **8**, 100 (2017).
56. Stroud, H., Feng, S.H., Kinney, S.M., Pradhan, S. & Jacobsen, S.E. 5-Hydroxymethylcytosine is associated with enhancers and gene bodies in human embryonic stem cells. *Genome biology* **12** (2011).
57. Tan, L., *et al.* Genome-wide comparison of DNA hydroxymethylation in mouse embryonic stem cells and neural progenitor cells by a new comparative hMeDIP-seq method. *Nucleic acids research* **41**, e84 (2013).
58. Szulwach, K.E., *et al.* Integrating 5-hydroxymethylcytosine into the epigenomic landscape of human embryonic stem cells. *PLoS genetics* **7**, e1002154 (2011).
59. Bernstein, B.E., *et al.* A bivalent chromatin structure marks key developmental genes in embryonic stem cells. *Cell* **125**, 315-326 (2006).
60. Pastor, W.A., *et al.* Genome-wide mapping of 5-hydroxymethylcytosine in embryonic stem cells. *Nature* **473**, 394-397 (2011).
61. Williams, K., *et al.* TET1 and hydroxymethylcytosine in transcription and DNA methylation fidelity. *Nature* **473**, 343-348 (2011).
62. Wu, H., *et al.* Dual functions of Tet1 in transcriptional regulation in mouse embryonic stem cells. *Nature* **473**, 389-393 (2011).
63. Yildirim, O., *et al.* Mbd3/NURD complex regulates expression of 5-hydroxymethylcytosine marked genes in embryonic stem cells. *Cell* **147**, 1498-1510 (2011).
64. Neri, F., *et al.* Genome-wide analysis identifies a functional association of Tet1 and Polycomb repressive complex 2 in mouse embryonic stem cells. *Genome biology* **14**, R91 (2013).
65. Khoueiry, R., *et al.* Lineage-specific functions of TET1 in the postimplantation mouse embryo. *Nature genetics* **49**, 1061-1072 (2017).
66. Butt, A.M. Neurotransmitter-mediated calcium signalling in oligodendrocyte physiology and pathology. *Glia* **54**, 666-675 (2006).
67. Friess, M., *et al.* Intracellular ion signaling influences myelin basic protein synthesis in oligodendrocyte precursor cells. *Cell Calcium* **60**, 322-330 (2016).
68. Li, T., *et al.* Dynamic Calcium Release From Endoplasmic Reticulum Mediated by Ryanodine Receptor 3 Is Crucial for Oligodendroglial Differentiation. *Frontiers in molecular neuroscience* **11**, 162 (2018).
69. Zhang, M., Liu, Y., Wu, S. & Zhao, X. Ca(2+) Signaling in Oligodendrocyte Development. *Cell Mol Neurobiol* **39**, 1071-1080 (2019).
70. Yu, Y., *et al.* Olig2 targets chromatin remodelers to enhancers to initiate oligodendrocyte differentiation. *Cell* **152**, 248-261 (2013).
71. Futatsugi, A., *et al.* IP3 receptor types 2 and 3 mediate exocrine secretion underlying energy metabolism. *Science* **309**, 2232-2234 (2005).
72. Zhao, X., *et al.* MicroRNA-mediated control of oligodendrocyte differentiation. *Neuron* **65**, 612-626 (2010).

73. Chan, J.R., *et al.* NGF controls axonal receptivity to myelination by Schwann cells or oligodendrocytes. *Neuron* **43**, 183-191 (2004).
74. Evans, R.D., Weston, D.A., McLaughlin, M. & Brown, A.M. A non-linear regression analysis method for quantitative resolution of the stimulus-evoked compound action potential from rodent optic nerve. *Journal of neuroscience methods* **188**, 174-178 (2010).
75. Vorhees, C.V. & Williams, M.T. Morris water maze: procedures for assessing spatial and related forms of learning and memory. *Nat Protoc* **1**, 848-858 (2006).
76. Down, T.A., *et al.* A Bayesian deconvolution strategy for immunoprecipitation-based DNA methylome analysis. *Nature biotechnology* **26**, 779-785 (2008).

Materials and Methods

Animals, immunohistochemistry and electron microscopy

All animal experiment protocols were approved by the Animal Care and Use Committee of the Fourth Military Medical University and were conducted in accordance with the guidelines for the care and use of laboratory animals. *Tet1* $^{flox/flox}$ mice [24] and *Tet3* $^{flox/flox}$ mice [18] were crossed with heterozygous *Olig1*-Cre mice [25, 70] to generate *Tet1*$^{flox/+}$;*Olig1*Cre$^{+/-}$ mice and *Tet3*$^{flox/+}$;*Olig1*Cre$^{+/-}$ mice, which were then bred with *Tet1*$^{flox/flox}$ mice or *Tet3*$^{flox/flox}$ to produce *Tet1* cKO (*Tet1*$^{flox/flox}$;*Olig1*Cre$^{+/-}$) or *Tet3* cKO (*Tet3*$^{flox/flox}$;*Olig1*Cre$^{+/-}$) offspring, respectively. *NG2CreER*^{T} mice [33] were from Jackson lab. *Itpr2* $^{flox/flox}$ line [71] was provided by the RIKEN BRC (RBRC10293) through the National Bio-Resource Project of the MEXT/AMED, Japan. It was crossed with heterozygous *Olig1*-Cre mice to generated *Itpr2* cKO (*Itpr2* $^{flox/flox}$;*Olig1*Cre$^{+/-}$) as stated above.

For immunohistochemistry, cryosections (14μm) of brains or spinal cords were short-fixed 30 min in 4% paraformaldehyde and processed for antigen retrieval. Sections were treated with 10mM sodium citrate (pH6.0) at ~90°C for 10min in a microwave and cooled down in room temperature. Then sections were washed three times in PBS, blocked in 3% BSA with 0.03% Triton X-100 (blocking buffer) for 1 hour (hr) at RT, and incubated with primary antibodies in blocking buffer overnight at RT. Next day, sections were washed three times in PBS, incubated with secondary antibodies at RT for 2 hr, and then counter stained with DAPI for 5min. Finally, sections were washed three times in PBS and mounted. Images were taken on Olympus FV1200 Confocal microscope. We used antibodies against Olig2 (Millipore, AB9610), Sox10 (Santa Cruz, 17342), TET1 [16], PDGFRα (Abcam, ab61219), CC1 (Oncogene Research, OP80), MBP (Abcam, ab7349), 5hmC (Active motif, 39769), ALDHL1 (Proteintech, 17390-1-AP), CNPase (Sigma, C5922), Ki67 (Abcam, ab16667), GFAP (Millipore, mAB360), GST-pi (Abcam, ab53943), DCX (Millipore, ab2253), Itpr2 (Millipore, AB3000).

For BrdU pulse labeling, animals were injected intraperitoneally with 100 mg BrdU/kg body weight 2 hr prior to sacrifice. For the staining of BrdU, as well as 5hmC, before permeabilization, sections were subjected to DNA denaturation with 2N hydrochloric acid at 37 °C for 20 min and then neutralized with 0.1 M sodium borate at pH 8.5 for 2X 10 min. The G3G4 monoclonal antibody (anti BrdUrd) was obtained from the Developmental Studies Hybridoma Bank developed under the auspices of the NICHD and maintained by The University of Iowa.

For TUNEL/Olig2 double staining, Olig2 immunostaining were applied after DeadEnd™ Fluorometric TUNEL System kit (Promega, G2350) to reveal TUNEL positive cells in OL lineage.

For electron microscopy, tissues were dissected and fixed in 2% glutaraldehyde and 4% paraformaldehyde in 0.1 M cacodylate buffer (pH 7.2) for 24 hr and processed as previously described [72]. Ultrathin sections were examined under the JEM-1230 electron microscope (JEOL LTD, Tokyo, Japan) equipped with CCD camera and its application software (832 SC1000, Gatan, Warrendale, PA).

Western blot assay

Immunoblotting were performed as described previously by our lab [16]. We used antibodies against Olig2 (Millipore MABN50), MBP (Abcam, ab7349), NeuN (Abcam, ab7349), ALDHL1 (Proteintech, 17390-1-AP), DCX (Proteintech, 13925-1-AP), β-actin (GuanXingYu, P1001) and Tubulin (Abbkine, A01030). The band intensity was calculated with Tanon5200 imager, normalized to β-actin or Tubulin level expressed as relative fold change against control.

RNA Extraction and qRT-PCR

Total RNAs were purified from tissues or cell cultures using TRIzol reagent according to the manufacturer's instruction (Invitrogen). For qRT-PCR, RNA was transcribed to cDNA with the PrimeScript™ RT reagent Kit (Perfect Real Time, Takara) and reactions were performed with SYBR® Premix Ex Taq™ (Takara) in CFX96 Touch Real-Time PCR Detection System (Bio-Rad). Relative gene expression was normalized to internal control β-actin. Primer sequences for SybrGreen probes of target genes are listed below.

Gene	Forward	Reverse
Ccna2	TGGATGGCAGTTTTGAATCACC	CCCTAAGGTACGTGTGAATGTC
Ccnb2	GCCAAGAGCCATGTGACTATC	CAGAGCTGGTACTTTGGTGTTC
Ccnf	AGAGACTGAATACGGGTTCTGA	TCCCAAGCAGTGTAGTATGGAA
Ccng2	AGGGGTTCAGCTTTTCGGATT	AGTGTTATCATTCTCCGGGGTAG
Cdc25b	TCCGATCCTTACCAGTGAGG	GGGCAGAGCTGGAATGAGG
Cdc25c	GGCAAACCTAAGCATTCTGTCG	CCAGAGGTCCAGATGAATCCA
Cdca3	CTGAGCGAAGTATTGGAGACAG	CTGCGGATTGTTTGGCTTCC
Cdk19	GGTCAAGCCTGACAGCAAAGT	TTCCTGGAAGTAAGGGTCCTG
Cldn11	ATGGTAGCCACTTGCCTTCAG	AGTTCGTCCATTTTTCGGCAG
Enpp2	TTTGCACTATGCCAACAATCGG	GGAGGCACTTTAGTCCTGTACTT
Kif11	GGCTGGTATAATTCCACGCAC	CCGGGGATCATCAAACATCTG
Mbp	GCAGCCAGCACCACTCTTGA	CAGCCGAGGTCCCATTGTTC
Myrf	CCTGTGTCCGTGGTACTGTG	TCACACAGGCGGTAGAAGTG
Cnp	TTTACCCGCAAAAGCCACACA	CACCGTGTCCTCATCTTGAAG
Ugt8a	ACTCCATATTTCATGCTCCTGTG	AGGCCGATGCTAGTGTCTTGA
Plp1	CCAGAATGTATGGTGTTCTCCC	GGCCCATGAGTTTAAGGACG
Bcas1	AGAAGCGAAAGGCTCGGAAG	AGGGACAGAATAACTCAGAGTGT
Tet1	CATTCTCACAAGGACATTCACAACA	AGTAAAACGTAGTCGCCTCTTCCTG
β-actin	GGCTGTATTCCCCTCCATCG	CCAGTTGGTAACAATGCCATGT
Ccl22	AGGTCCCTATGGTGCCAATGT	CGGCAGGATTTTGAGGTCCA
Ccl2	TCAAACTGAAGCTCGCACTCT	GGGGCATTGATTGCATCTGG
Ccr2	ATCCACGGCATACTATCAACATC	CAAGGCTCACCATCATCGTAG
Cx3cr1	GAGTATGACGATTCTGCTGAGG	CAGACCGAACGTGAAGACGAG
Itpr2	CCTCGCCTACCACATCACC	TCACCACTCTCACTATGTCGT
Cacna1a	CACCGAGTTTGGGAATAACTTCA	ATTGTGCTCCGTGATTTGGAA
Cacna1c	ATTGTGCTCCGTGATTTGGAA	ACTGACGGTAGAGATGGTTGC
Cacna2d1	GTCACACTGGATTTTCTCGATGC	GGGTTTCTGAATATCTGGCCTGA
Cacnb4	TACCTGCATGGAGTTGAAGACT	TTCGCTCTCTCAAGCTGGATA
Cacng5	ACCTGGAAGAAGGCATAATCCT	CTATGGTAAAACAGCGTCCTCG
Atp2b1	AGATGGAGCTATTGAGAATCGCA	CCCTGTAACACGGATTTTTCCTT
Atp2c1	GCAGGCAGAAGAAGCACCAA	CCTAGTAACCAGCCAACCAAC

Slc8a1	CTTCCCTGTTTGTGCTCCTGT	AGAAGCCCTTTATGTGGCAGTA

Culture of OL precursor cells, immunocytochemistry and ELISA assay

Mouse OPCs were isolated from P6 cortices of mice by immunopanning with antibodies against Ran-2, GalC and O4 sequentially as previously described [73]. Briefly, cerebral hemispheres were diced and digested with papain at 37°C. Following gentle trituration, cells were resuspended in a panning buffer containing insulin (5 μg/ml) and then incubated at room temperature sequentially on three immunopanning dishes: Ran-2, anti-GalC, and O4. $O4^{+}GalC^{-}$ OPCs were released from the final panning dish with trypsin (Sigma).

For immunocytochemistry, cell cultures were fixed in 4% PFA. After TritonX-100 permeabilization for 15 min, samples were incubated with primary antibody for 1 h at room temperature followed by fluorescent secondary antibody for another hour. Cells were then counter-stained with DAPI and visualized with Confocal microscope. Experiments were replicated using cells from three different primary cultures.

Flow cytometric analysis of cell cycle with propidium iodide DNA staining

PI staining for flow cytometry was performed according to the user manual of DNA Content Quantitation Assay (Cell Cycle) from Solarbio (#CA1510). Briefly, OPCs from control or *Tet1* cKO mice were harvested, washed in PBS and fixed in cold 70% ethanol for 30 min at 4°C. After wash twice in PBS, cells were treated with RNase and then stained with PI. With guava easyCyte6HT (Millipore), the forward scatter (FS) and side scatter (SS) were measured to identify single cells. For analysis, ModFit LT software was used make the PI histogram plot. Experiments were replicated three times.

Lysolecithin-induced demyelinating injury

Lysolecithin-induced demyelination was carried out in the corpus callosum of 8-week-old mice. Anesthesia was induced and maintained by peritoneal injection of a mixture of ketamine (90 mg/kg) and xylazine (10 mg/kg). The skull was exposed, and a hole was cut into the cranium. Focal demyelinating lesions were induced by stereotaxic injection of 0.8 μl 1%lysolecithin solution (L-a-lysophosphatidylcholine, Sigma L4129) into the corpus callosum at coordinates: 0.8 mm lateral, 0.8 mm rostral to bregma, 1.2mm deep to brain surface) using a glass-capillary connected to a 10 μl Hamilton syringe. Animals were left to recover in a warm chamber before being returned into their housing cages. LPC-induced injuries were conducted in a genotype-blinded manner.

Electrophysiology

Analyzing the compound action potential was performed according to previous protocols [27, 74]. *Tet1* cKO and control littermates were killed by cervical dislocation and then decapitated. Optic nerves were dissected free and cut between the orbit and the optic chiasm in the standard artificial cerebrospinal fluid (aCSF) containing (in mM): NaCl 126, KCl 3.0, $CaCl_2$ 2.0, $MgCl_2$ 2.0, NaH_2PO4 1.2, $NaHCO_3$ 26 and glucose 10 at 37℃. Following dissection, optic nerves were equilibrated in aCSF for at least 30 min with constant aeration (95% O_2/5% CO_2). Then the nerve was gently placed in a customized perfusion chamber, maintained at 37℃ and perfused with aCSF at 2-3ml/min speed. Suction electrodes back-filled with aCSF were used for stimulation and recording. One electrode was attached to the rostral end of the nerve for stimulation and the second suction electrode was attached to the caudal end of the nerve to record the CAP, thus all recordings were orthodromic. Stimulus pulse strength (100μs duration, SS-201J Isolator constant current output with SEN-7203 stimulator, Nihon Kohden, Japan) was adjusted to evoke the maximum CAP possible and then increased another 25% (i.e. supramaximal stimulation). During an experiment, the supra maximal CAP was elicited every 10s and repeat 10 times. The signal was amplified 100×AC membrane potential (100mV/mV) by a Multiclamp700B amplifier, filtered at 10 kHz and acquired at 10 kHz (Digidata 1322A, Molecular Devices, USA). The average CAP amplitude and area were measured in Clampfit 10.0 software (Molecular Devices, USA) offline and performed blind to genotype. Image drawing and statistical analysis were performed in

GraphPad Prism 6.

Behavior test

Startle response/prepulse inhibition tests

A startle reflex measurement system was used to measure startle response and prepulse inhibition. Throughout the session, the startle system delivered a constant background white noise of 68 dB. The startle response was recorded for 300 ms (measuring the response every 1 ms) with the onset of stimulus and a startle response was defined as the peak response during the 300 ms period.

Acoustic startle began by placing a mouse in the undisturbed chamber for 5 min. The test consists ten 20-ms bursts of white noise varied in level from 65-125 dB sound stimuli in steps of 5dB, plus ten no-stimulus trials. The order of these stimuli was randomized, and the duration of inter-trial intervals was 15 s. The prepulse inhibition test session began with a 5 min acclimation period followed by three consecutive blocks of test trials. Block 1 and 3 consisted of six startle stimulus-alone trials. Block 2 contained 10 startle stimulus-alone trials, 10 prepulse + startle trials per prepulse intensity, and 10 no-stimulus trials. Three combinations of prepulse and startle stimuli (70-120, 76-120 and 82-120 dB) were employed. Trials were presented in a pseudo-random order, ensuring that each trial was presented 10 times and that no two consecutive trials were identical. Inter-trial intervals ranged from 30 to 45 s. Basal startle amplitude was determined as the mean amplitude of the 10 startle stimulus-alone trials. PPI was calculated according to the formula: $100 \times [1-(PPx/P120)]$ %, in which PPx means the 10 PPI trials (PP70, PP76 or PP82 and P120 was the basal startle amplitude).

Morris Water Maze:

The Morris water maze was conducted as described [75] with minor modifications. A white plastic tank 120 cm in diameter was kept in a fixed position and filled with 22°C water, which was made opaque with milk. A 10 cm platform was submerged 1cm below the surface of opaque water and located in the center of one of the four virtually divided quadrants. All animal activities were automatically recorded and measured by a video-based Morris water maze tracking system. The swim training consisted of 5 days of trials, during each day mice were released from four random locations around the edge of the tank with an inter-trial interval of about 30 min and they were allowed to freely swim for a maximum of 60 sec or guided to the platform. Afterwards, mice were allowed to stay on the platform for 15 sec. A probe trial was performed 24 h after the last day of training. During the probe trial, mice were allowed to swim in the pool without the escape platform for 60 s. The performance was expressed as the percentage of time spent in each quadrant of the MWM and swim distance in the target quadrant, which were automatically recorded. Moreover, the latency to reach the platform position (using 10 cm diameter) and the number of crossings through the position were manually recorded.

RNA-Seq and Data Analysis

RNA-seq assays were performed by RiboBio Co., Ltd. (Guangzhou, China). Briefly, libraries were prepared using Illumina RNA-Seq Preparation Kit (TruSeq RNA Sample Prep Kit) and sequenced by HiSeq 3000 sequencer. RNA-seq reads were mapped using TopHat with settings of “read mismatches=2” and “read gap length=2” (http://ccb.jhu.edu/software/tophat/ index.shtml). TopHat output data were then analyzed by DEGseq to compare the changes of gene expression between *Tet1 cKO* and control, based on the calculate RPKM values for known transcripts in mouse genome reference. Heatmap of gene differential expression was generated using R Package (http://www.r-project.org).

hMeDIP-Sequencing analysis

hMeDIP Sequencing service was provided by KangChen Biotech (Shanghai, China). hMeDIP-Sequencing library preparation was performed according to a previous study[76] with minor modifications. Genomic DNA was sonicated to ~200-800bp with a Bioruptor sonicator (Diagenode). 800 ng of sonicated DNA was end-repaired, A-tailed, and ligated to single-end

adapters following the standard Illumina genomic DNA protocol (FC-102-1002, Illumina). After agarose size-selection to remove unligated adapters, the adaptor-ligated DNA was used for immunoprecipitation (IP) with a mouse monoclonal anti-5-hydroxymethylcytosine antibody (Diagenode, C15200200). For this, DNA was heat-denatured at 94°C for 10 min, rapidly cooled on ice, and immunoprecipitated with 1 μL primary antibody overnight at 4°C with rocking agitation in 400 μL IP buffer (0.5% BSA in PBS). To recover the immunoprecipitated DNA fragments, 20 μL of magnetic beads were added and incubated for an additional 2 hours at 4°C with agitation. After IP, a total of five washes were performed with ice-cold IP buffer. Washed beads were resuspended in TE buffer with 0.25% SDS and 0.25 mg/mL proteinase K for 2 hours at 65°C and then allowed to cool down to room temperature. DNA was then purified using Qiagen MinElute columns and eluted in 16 μL EB (Qiagen). 14 cycles of PCR were performed on 5 μL of the immunoprecipitated DNA using the single-end Illumina PCR primers. The resulting products were purified with Qiagen MinElute columns, after which a final size selection (300-1,000 bp) was performed by electrophoresis in 2% agarose. Libraries were quality controlled by Agilent 2100 Bioanalyzer.

For sequencing, the library was denatured with 0.1 M NaOH to generate single-stranded DNA molecules and loaded onto channels of the flow cell at 8 pM concentration, amplified in situ using TruSeq Rapid SRCluster Kit (GD-402-4001, Illumina). Sequencing was carried out by running 150 cycles on Illumina HiSeq 2500 using TruSeq Rapid SBS Kit (FC-402-4001, Illumina) according to the manufacturer's instructions.

After sequencing images generated, the stages of image analysis and base calling were performed using Off-Line Base caller software (OLB V1.8). After passing Solexa CHASTITY quality filter, the clean reads were aligned to Mus_musculus genome (UCSC mm10) using BOWTIE software (V2.1.0). Aligned reads were used for peak calling, both mRNA and LncRNA associated hMeDIP enriched regions (peaks) with statistically significant were identified for each sample, using a q-value threshold of 10^{-4} by MACS v2. Both mRNA and LncRNA associated hMeDIP enriched regions (peaks) were annotated by the nearest gene using the newest UCSC RefSeq database. Differentially hydroxymethylated regions (DhMRs) between two groups with statistically significant were identified by diffReps (Cut-off: $log_2FC=1.0$, p-value=10^{-4}). DhMRs were annotated by the nearest gene using the UCSC RefSeq and database of multiple databases integration.

$[Ca^{2+}]_i$ imaging

Fluo4 was used to measure $[Ca^{2+}]i$ changes. To load cells with Ca^{2+} probe, cultures were incubated in standard artificial cerebrospinal fluid (aCSF) containing (in mM): NaCl 125, KCl 3.0, $CaCl_2$ 2.0, $MgCl_2$ 2.0, NaH_2PO4 1.25, $NaHCO_3$ 26 and glucose 20, or calcium free aCSF (NaCl 125, KCl 3.0, MgCl2 2.0, MgSO4 2.0, NaH2PO4 1.25, NaHCO3 26, glucose 20, HEPES 10 and EGTA 10 (pH 7.4)), supplemented with 0.03% Pluronic F-127 and 0.6μM cell-permeable form of indicator (Fluo4-AM, Invitrogen) for 20 min at 37℃. After loading, cells were transferred into recording chamber on the stage of Olympus FV1000 confocal inverted microscope equipped with phase contrast optics. Measurements started after at least 15 min storage in aCSF to ensure deesterification of indicators. Fluo4 was excited with 488 nm laser and emitted light was collected at 515 nm. A series of sections were collected every 500 ms, at 500 ms intervals, for 180 s in total. Pharmacological agents were directly added in aCSF: ATP (Sigma, 100μM) or Bay K 8644 (10 μM), 30s after the first image was taken. The images were analyzed using the Olympus FV10-ASW 4.1 software. Cell bodies were selected as regions of interest (ROI) and normalized changes of Fluo4 fluorescence intensities were calculated as $\Delta F/F=(F-F0)/F0$ (F, fluorescence intensity; $F0$, baseline intensity). Data were expressed as Mean ± Standard Deviation (SD), 'N' represents the number of responding cells. Experiments were performed 3 times from different cultures and the results were pooled together for analysis. N>100 in ATP treatment group and N>70 in Bay K 8644 group.

Duplex siRNA transfection

For in vitro *Itpr2* knockdown, purified OPCs were transfected with 50 nM duplex siRNA against

Itpr2 (sense, 5' GGUACCAGCUAAACCUCUUTT 3'; anti-sense, 5' AAGAGGUUUAGCUGGUAC CTT 3') or control nontargeting siRNA (Genepharma, Shanghai) using Lipofectamine RNAiMAX (Invitrogen). Six hours after transfection, the cultures were changed to differentiation medium. Two or four days later, cultures were harvested for qRT-PCR assay or immunocytochemistry as indicated.

Statistical analysis

Numerical values were analyzed using Mean ± SEM and are presented as bar graphs. Group meet normal distribution and homogeneity of variance were compared using Two-tailed unpaired *t*-test. Group with normal distribution but do not meet homogeneity of variance were compared using Two-tailed unpaired separate variance estimation *t*-test. Group do not meet normal distribution were compared using Mann-Whitney U test. Two factors do not meet normal distribution or homogeneity of variance using Friedman M test. RMANOVA with repeated measures were applied to the data when appropriate with SPSS22.0. Significance is denoted as $^{*}p<0.05$, $^{**}p<0.01$ or $^{***}p<0.001$ in the figures.

Data availability

The transcriptome and DNA hydroxymethylation profiling dataset have been deposited in the Gene Expression Omnibus database (GSE122838).

Figure legends

Fig. 1 Dynamic 5hmC expression pattern during OPC specification

(a) Venn diagram of hydroxymethylated genes in NPCs and OPCs.
(b) Gene ontology analysis of genes with OPC-specific 5hmC peaks in promoter or TSS regions.
(c) GSEA plots of gene terms involved in “bipotent progenitor”, “oligodendrocyte progenitor”, “postmitotic oligodendrocyte” and “pluripotent stem cells” for genes with 5hmC peaks in gene body region from NPCs and OPCs.
(d) Snapshots of 5hmC profiles of representative OPC-associated genes, *Cspg4* and *Slc22a3*, in NPCs and OPCs.
(e) Snapshots of 5hmC profiles of representative immature oligodendrocyte (iOL)-associated genes, *Tmem141* and *Kndc1*, in NPCs and OPCs.
(f) Snapshots of 5hmC profiles of representative mature oligodendrocyte (mOL)-associated genes, *Mag* and *Elovl7*, in NPCs and OPCs.
(g) Snapshots of 5hmC profiles of representative negative regulators of oligodendrocyte differentiation, *Id2* and *Zfp28* in NPCs and OPCs.

Fig. 2 TET1 is required for OL differentiation and myelination

(a) Schematic diagram of Cre-mediated excision of floxed *Tet1* exons encoding the critical catalytic domain for dioxygenase activity (modified from Zhang et al., 2013).
(b) Representative immunostaining for TET1 expression in P4 corpus collosum from control and *Tet1* cKO mice. Upper images show TET1 (green), Sox10 (red), and DAPI (blue) staining. Lower images show only TET1. Arrows indicate Sox10$^+$ cells. Scale bar, 20 μm.
(c) Percentage of TET1$^+$ cells among Sox10$^+$ oligodendrocytes in P4 corpus collosum of control and *Tet1* cKO mice. Data are Means ± SEM (n=4 animals each group). ***, p<0.001, Student’s *t* test.
(d) Representative images of CC1 and Sox10 immunostaining in the corpus callosum of control and *Tet1* cKO mice at P8. Scale bar, 50 μm.
(e) Quantification of CC1$^+$ cells in P8, P21, and P27 and P60 control and *Tet1* cKO corpus collosum (n=4 animals each group). *, p<0.05, **, p<0.01, compared to control, Student’s *t* test.
(f) Representative images of MBP immunostaining in *Tet1* cKO and control mice cortex (upper images) and corpus collosum (lower images) at P16. Scale bar, 100 μm.
(g) Representative electron micrographs of optic nerve at P14 and corpus callosum at P27 from control and *Tet1* cKO mice. Scale bar, 0.5 μm in P14 and 2 μm in P27.
(h) Quantification the number of myelinated axons in defined areas from optic nerve of control and *Tet1* cKO mice. Data are Means ± SEM (n=6 slides from 3 animals per group). ***, p<0.001 compared to control, Student’s *t* test.
(i) G ratios versus axonal perimeters for P14 optic nerve in control and *Tet1* cKO mice. p<0.001, Friedman M test (> 150 myelinating axon counts/animal from 3 animals/genotype).
(j) Quantification the number of myelinated axons in defined areas from corpus callosum of control and *Tet1* cKO mice. Data are Means ± SEM (n=6 slides from 3 animals per group). ***, p<0.001 compared to control, Student’s *t* test.
(k) G ratios versus axonal perimeters for P27 corpus callosum in control and *Tet1* cKO mice. p=0.002, Student’s *t* test (> 120 myelinating axon counts/animal from 3 animals/genotype).
(l) Representative CAP series from optic nerves of control and *Tet1* cKO mice elicited by square voltage pulses of varied amplitudes.
(m) Evoked CAP amplitudes of the 2nd peak (maximal) from control and *Tet1* cKO mice plotted versus stimulus intensities. Data are Means ± SEM (n=9 nerves per group). **, p<0.01 compared to control by Student’s *t* test.
(n) Total CAP area vs. stimulus intensities in controls and *Tet1* cKO mice at all stimulus intensities compared. Data are Means ± SEM (n=9 nerves per group). **, p<0.01 compared to control by Student’s *t* test.

Fig. 3 Proliferation and cell-cycle progression are defective in OPCs from *Tet1* cKO mice

(a) Representative images of Olig2 staining for E15.5 and Sox10/ PDGFRα staining for P1 control and *Tet1* cKO cortexes. Scale bar, 100 μm.
(b) Quantification of Olig2$^+$ cells in cortexes from E15.5 and P1 controls and *Tet1* cKO mice. Data are Means ± SEM (n=4 animals per group). *, p<0.05 compared to control, Mann-Whitney U test，*** p<0.001 compared to control, Student's *t* test.
(c) Quantification of PDGFRα$^+$ cells in cortexes from E15.5, P1, P6, P14, and P60 controls and *Tet1* cKO mice. Data are Means ± SEM (n=3 animals per group) *, p<0.05 compared to control, Student's *t* test.
(d) Representative images of P1 control and *Tet1* cKO cortexes immunostained for BrdU and Olig2. Scale bar, 100 μm.
(e) Quantification of BrdU$^+$ cells within Olig2$^+$ OPC population in control and *Tet1* cKO brains. Data are Means ± SEM (n=3 animals per group). *, p<0.05 compared to control, Student's *t* test.
(f) Representative flow cytometry traces of propidium iodide-stained OPCs from control and *Tet1* cKO mice.
(g) Quantification the percentage of OPCs from control and *Tet1* cKO mice in each phase of the cell cycle. Data are Means ± SEM (n=3~4 independent cultures per group). **, p<0.01 compared to control, Mann-Whitney U test.
(h) Representative images of immunostaining of CNPase and MBP at 3 days *in vitro* (3DIV) and 5 DIV after induction of differentiation in control and *Tet1* cKO cultures. Scale bar, 50 μm.
(i) Density of CNPase$^+$ and/or MBP$^+$ cells in cultures from control or *Tet1 cKO* mice. Data are Means ± SEM (n=4 of independent experiments each group). ***, p<0.001, Student's *t* test.

Fig 4. OPC differentiation is impaired in *Tet1* OPC-iKO mice
(a) Diagram showing TAM administration to induce the Cre recombination in *Tet1* OPC-iKO (*NG2-CreER*^{T}: *Tet1*$^{flox/flox}$) mice.
(b) Representative images of P7 control and *Tet1*-iKO mice corpus collosum stained for TET1 and Sox10. Arrows indicate Sox10$^+$ cells that show reduced levels of TET1 in *Tet1*-iKO image. Scale bar, 20 μm.
(c) Percentages of TET1$^+$ cells among Sox10$^+$ oligodendrocytes in P7 corpus collosum. Data are Means ± SEM (n=4 animals per group). **, p<0.01 compared to control by Student's *t* test.
(d) Representative images of control and *Tet1* OPC-iKO P7 corpus callosum stained for PDGFRα/Ki67 or MBP. Scale bar, 100 μm.
(e-g) Quantification the density of PDGFRα$^+$ cells (e), the percentage of Ki67$^+$ cells among PDGFRα$^+$ cells (f) and the density of MBP$^+$ cells at P7 (g). * p<0.05, compared to control by Student's *t* test (n=3 animals per group).
(h) Representative images of control and *Tet1* OPC-iKO P14 corpus callosum stained for CC1/Sox10 and MBP. Scale bar, 100 μm.
(i) Quantification the density of CC1$^+$ cells at P14. *** p<0.001 compared to control by Student's *t* test (n=3 animals per group).

Fig. 5 Impaired CNS remyelination in *Tet1* OPC-iKO mice
(a) Diagram of brain showing the LPC injection site.
(b) Representative images of TET1 immunostaining in corpus callosum of non-lesion vehicle injection region and LPC-induced lesion region of wild-type mouse at dpl 7. Arrows indicate TET1$^+$/Olig2$^+$ cells. Scale bar, 50 μm.
(c) Quantification of TET1$^+$ cell density and the percentages of TET1$^+$ and Olig2$^+$ cells in LPC lesion sites at dpl 7. Data are presented as Means ± SEM (n=3~4 animals per group). * p<0.05, ***, p<0.001, Student's *t* test.
(d) Diagram showing TAM administration and LPC injection schedule in *NG2CreER*^{T};*Tet1*$^{flox/flox}$ mice.
(e) Representative images of lesion regions from control and *Tet1*-iKO mutants at dpl 7 and dpl 14. Samples were immunolabeled for PDGFRα and GST-pi, respectively. Dashed line indicates the border of lesion site. Scale bars, 100 μm.
(f) Quantification of PDGFRα$^+$ OPCs in LPC lesion sites at dpl 7. Data are Means ± SEM (n=3

animals each group). p = 0.848, Student's t test.
(g) Quantification of GST-pi$^+$ OLs in LPC lesion sites at dpl 14 and 21. Data are Means ± SEM (n=4 animals each group). * p<0.05, ***p<0.001, Student's t test.
(h) Contralateral side and LPC lesion regions from control and *Tet1*-iKO corpus callosum at dpl 21. Samples were immunostained for MBP. Scale bar, 200 μm.
(i) Representative images of electron micrographs of lesion regions from control and *Tet1*-iKO mutants at 28 dpl. Scar bar, 0.5 μm.
(j) The number of myelinated axons in lesion regions from control and *Tet1*-iKO mutants at 28 dpl. Data are Means ± SEM (n=4 slides from 3 animals per group). ***, p<0.001 compared to control, Student's t test.
(k) G ratios versus axonal perimeters in lesion regions from control and *Tet1*-iKO mutants at 28 dpl. p<0.001 compared to control, Student's t test (> 130 myelinating axon counts/animal from 3 animals/genotype).

Fig. 6 Lack of *Tet1* alters the transcriptome profiles in OPCs
(a) Heatmap of RNA-seq data from purified OPCs shows categories of differentially expressed genes between control and *Tet1* cKO mice. Each genotype was repeated once.
(b) GSEA analysis of the most differentially regulated genes in OPC cultures from *Tet1* mutant and control mice.
(c-f) GSEA plots of genes involved in oligodendrocyte differentiation (c), cell division (d), mitochondria genes (e) and chemokine signaling pathway genes (f) in control and *Tet1* mutant OPCs.
(g-i) Quantitative real-time PCR of oligodendrocyte differentiation genes (g), genes involved in cell division and G2/M cell cycle regulation (h), and chemokine genes (i) in control and *Tet1* mutant OPCs. Data are means ± SEM of transcript levels relative to control after normalization from three independent experiments each performed in triplicate. * p<0.05, ** p<0.01, *** p<0.001, compared to control, Student's t test.

Fig. 7 DNA hydroxymethylation of genes and transcript levels are correlated in oligodendrocytes from *Tet1* cKO mice
(a) Representative images of 5hmC and CC1$^+$ immunostaining in the corpus callosum of P27 control and *Tet1* cKO mice. Attenuated level of 5hmC in CC1$^+$ cells in *Tet1* mutant is indicated by arrows. Scale bar, 50 μm.
(b) Quantification the fluorescence intensity of 5hmC staining in CC1$^+$ cells from control and *Tet1* cKO brains. Data are Means ± SEM (n=4 animals per group) ***, p<0.001 compared to control, Student's t test.
(c) Normalized 5hmC tag density distribution from *Tet1* cKO and control OPCs.
(d) Heatmap of 5hmC signal from ±5 kb of TSS at all annotated genes in control and *Tet1* cKO OPCs.
(e) Quadrant plot of differentially hydroxymethylated peaks at gene bodies and differentially expressed genes (*Tet1* cKO versus Control, p<0.05). The x axis is Log_2 fold change of transcript level, and the y axis is the difference in DNA hydroxymethylation. Dashed lines indicate 2-fold difference. Genes indicated are involved in the OL differentiation, cell division and calcium transporter.
(f) Gene ontology analysis for downregulated and hypo-hydroxymethylated gene groups in *Tet1* ablated OPCs.
(g-h) 5hmC enriched genes involved in myelination (g) and calcium transport (h) from control (blue) and *Tet1* cKO (orange) OPCs.
(i) GSEA plots of genes involved in calcium ion transmembrane transporter activity in control and *Tet1* mutant OPCs.
(j) Quantitative real-time PCR of genes involved in calcium ion transmembrane transporter activity in control and *Tet1* cKO OPCs. Data are Means ± SEM of transcript levels relative to control after normalization from three independent experiments each performed in triplicate. ** p<0.01, *** p<0.001, compared to control, Student's t test.

Fig. 8 Impaired calcium transport in *Tet1* cKO OPCs and depletion of Itpr2, a TET1-5hmC target gene, inhibits developmental myelination

(a) Representative serial images obtained after addition of 100 μM ATP to OPCs from control or *Tet1* cKO mice.

(b) Representative traces of Fluo4 intensity in OPCs from control and *Tet1* cKO mice following application of ATP.

(c) Amplitude changes (ΔF/F) after ATP treatment of control and *Tet1* cKO OPCs. Data are Means ± SD (n=104-105 cells from three independent cultures). ***, $p<0.001$, Student's *t* test.

(d) The average rise in slope of Fluo4 intensity after ATP addition in control and *Tet1* cKO OPCs. Data are Means ± SD (n=104-105 cells from three independent cultures). ***, $p<0.001$, Student's *t* test.

(e) Representative images of Itpr2 immunostaining during OPC differentiation *in vitro*. Arrows indicate the highest level of Itpr2 in newly formed CNPase$^+$ oligodendrocytes from 1DIV differentiation cultures, which is not appear in other stages. Scale bar, 10 μm.

(f) Quantitative real-time PCR identified the efficiency of siRNA-*Itpr2* duplex in reducing the mRNA level of *Itpr2* in normal OPCs and in repressing the expression of two myelin genes, *Mbp* and *Plp*, in differentiating OLs, respectively. Transfection with non-targeting duplex was used as negative control (NC). Data are Means ± SEM (n=3 transfections). ** $p<0.01$, *** $p<0.001$, Student's *t* test.

(g) Immunostaining for MBP/Olig2 in OL cultures after transfected with siRNA-*Itpr2* duplex for 4 days. Scale bar, 100μm.

(h) Quantification the percentage of MBP$^+$ cells among Olig2$^+$ cells after siRNA transfection. Note the significant decrease of differentiated cells in siRNA-*Itpr2* transfected group. Data are Means ± SEM (n=3 transfections). * $p<0.05$, Student's *t* test.

(i) Representative double immunostaining for Itpr2 and Olig2 in P14 corpus collosum from control and *Itpr2* cKO mice. Scale bar, 50 μm.

(j) Percentage of Itpr2$^+$ cells among Olig2$^+$ OLs in P14 corpus collosum of control and *Itpr2* cKO mice. Data are Means ± SEM (n=4 animals each group). ***, $p<0.001$, Student's *t* test.

(k) Immunostaining for OPC marker PDGFRα and double immunostaining for OL lineage marker Olig2 and mature OL marker CC1 in corpus collosum from P14 *Itpr2* cKO mice. Scale bar, 50 μm.

(l) Quantification the percentage of PDGFRα$^+$ cells in P7 and P14 mice revealed significant reduction in *Itpr2* cKO mice. Data are Means ± SEM (n=4 animals per group). ** $p<0.01$, Student's *t* test.

(m) Quantification the percentage of CC1$^+$ cells among Olig2$^+$ cells from P7 to P31 mice revealed significant reduction in *Itpr2* cKO mice. Data are Means ± SEM (n=4 animals in control group and 3 animals in mutant). * $p<0.05$, Mann-Whitney U test, ** $p<0.01$, *** $p<0.001$, Student's *t* test.

(n) Representative images for MBP staining in corpus collosum from P31 *Itpr2* cKO mice. Scale bar, 50 μm.

(o) Representative electron micrographs of optic nerves from P16 control and *Itpr2* cKO mice. Scale bar, 1 μm.

(p) Quantification the number of myelinated axons in defined areas from optic nerves of control and *Itpr2* cKO mice. Data are Means ± SEM (n=8 slides from 3 animals per group). *** $p<0.001$ compared to control, Student's *t* test.

(q) G ratios versus axonal perimeters for control and *Itpr2* cKO mice reveal significant difference. $p<0.001$, compared to control, Friedman M test (> 110 myelinating axon counts/animal from 3 animals/genotype).

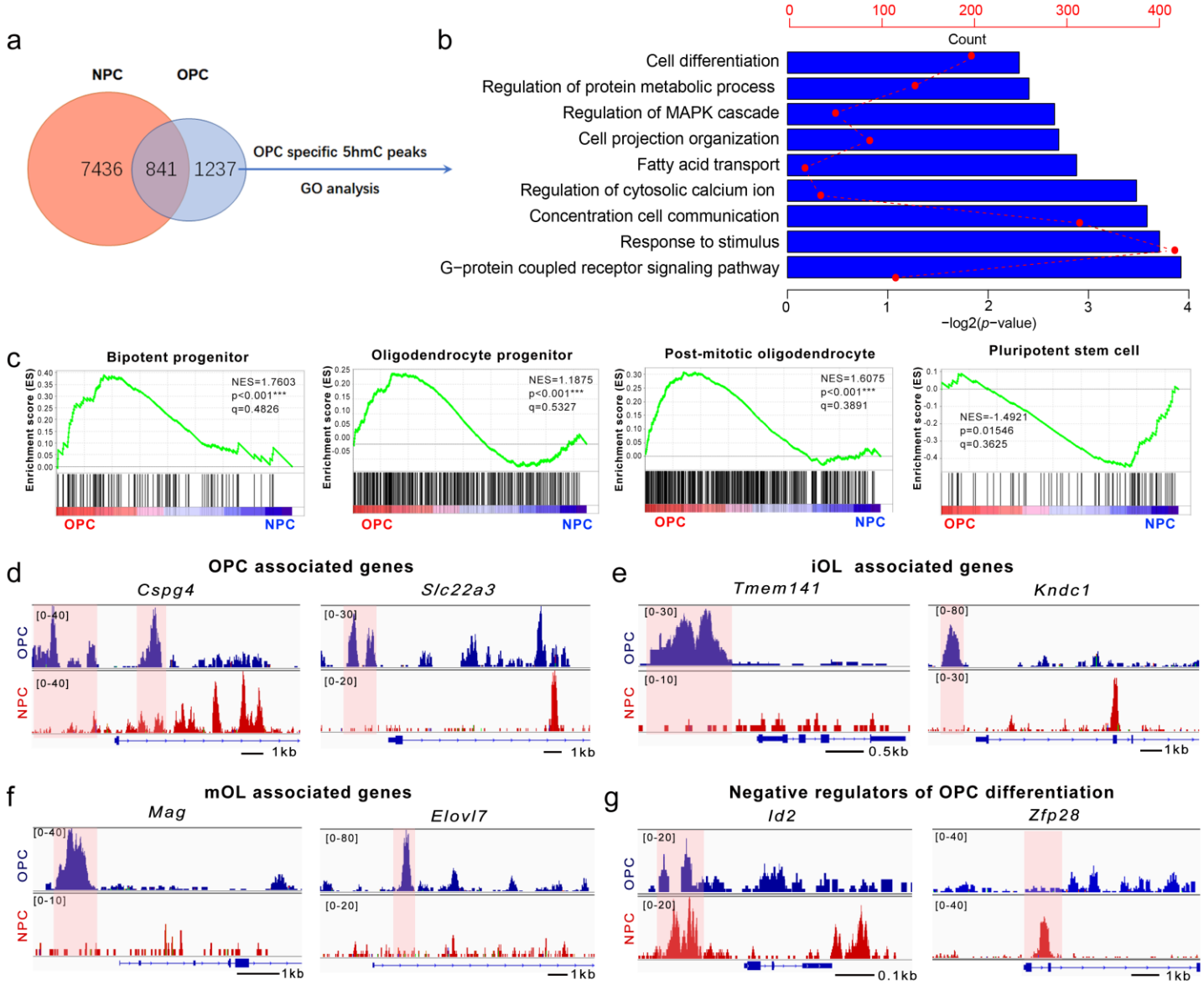
a
NPC
OPC
7436
841
1237
OPC specific 5hmC peaks
GO analysis
b
Count
Cell differentiation
Regulation of protein metabolic process
Regulation of MAPK cascade
Cell projection organization
Fatty acid transport
Regulation of cytosolic calcium ion
Concentration cell communication
Response to stimulus
G−protein coupled receptor signaling pathway
−log2(p−value)
c
Bipotent progenitor
NES=1.7603
p<0.001***
q=0.4826
Oligodendrocyte progenitor
NES=1.1875
p<0.001***
q=0.5327
Post-mitotic oligodendrocyte
NES=1.6075
p<0.001***
q=0.3891
Pluripotent stem cell
NES=-1.4921
p=0.01546
q=0.3625
Enrichment score (ES)
OPC
NPC
d
OPC associated genes
Cspg4
Slc22a3
e
iOL associated genes
Tmem141
Kndc1
f
mOL associated genes
Mag
Elovl7
g
Negative regulators of OPC differentiation
Id2
Zfp28
1kb
0.5kb
0.1kb

Figure 1

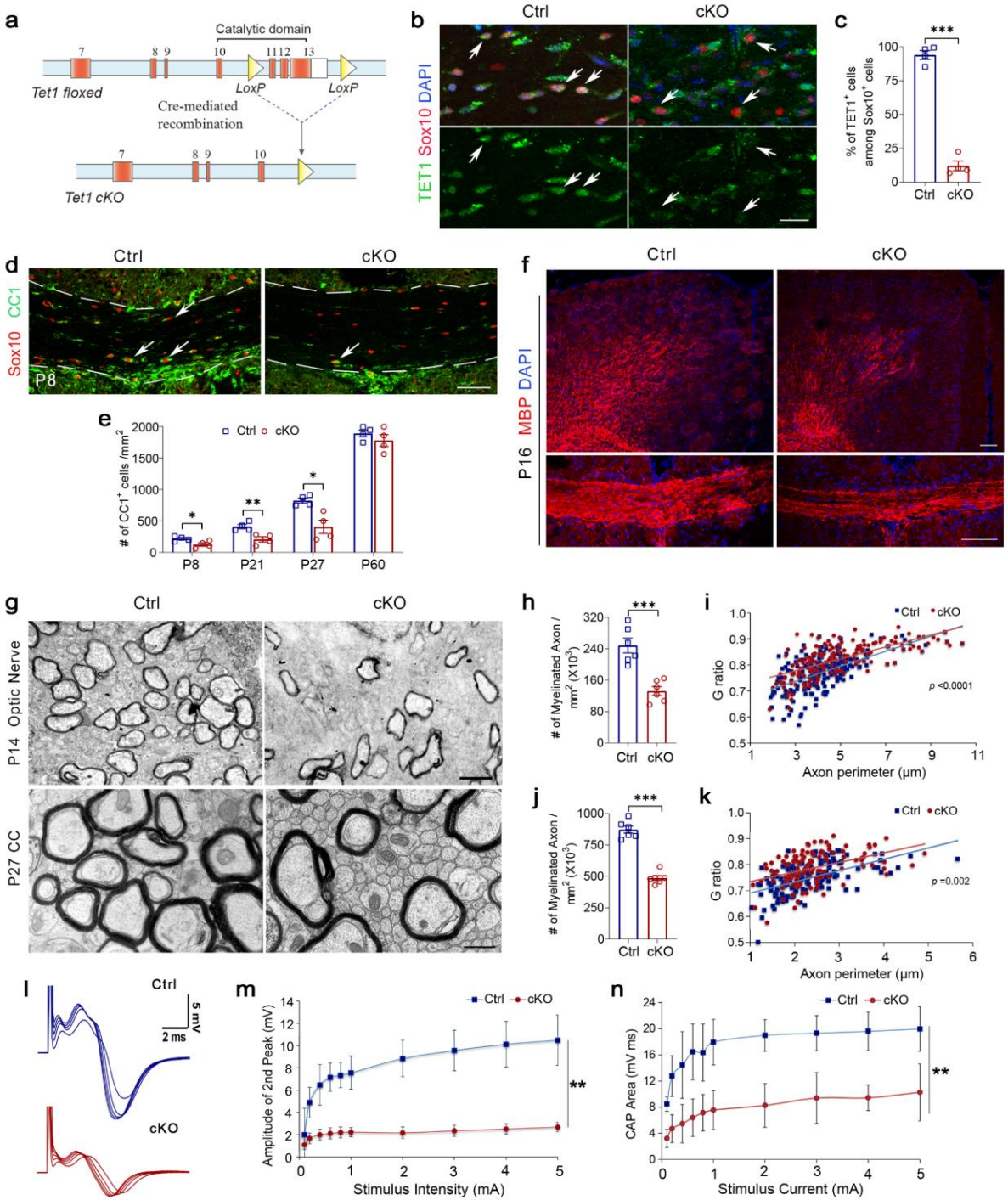
a
Catalytic domain
7
8 9
10
11 12
13
Tet1 floxed
LoxP
LoxP
Cre-mediated recombination
7
8 9
10
Tet1 cKO
b
Ctrl
cKO
TET1 Sox10 DAPI
c
***
% of TET1+ cells among Sox10+ cells
100
75
50
25
0
Ctrl
cKO
d
Ctrl
cKO
Sox10 CC1
P8
e
Ctrl cKO
# of CC1+ cells /mm2
2000
1500
1000
500
0
*
**
*
P8
P21
P27
P60
f
Ctrl
cKO
P16 MBP DAPI
g
Ctrl
cKO
P14 Optic Nerve
P27 CC
h
***
# of Myelinated Axon / mm2 (X10³)
320
240
160
80
0
Ctrl
cKO
i
Ctrl cKO
G ratio
p <0.0001
Axon perimeter (μm)
j
***
# of Myelinated Axon / mm2 (X10³)
1000
750
500
250
0
Ctrl
cKO
k
Ctrl cKO
G ratio
p =0.002
Axon perimeter (μm)
l
Ctrl
5 mV
2 ms
cKO
m
Ctrl cKO
Amplitude of 2nd Peak (mV)
**
Stimulus Intensity (mA)
n
Ctrl cKO
CAP Area (mV ms)
**
Stimulus Current (mA)

Figure 2

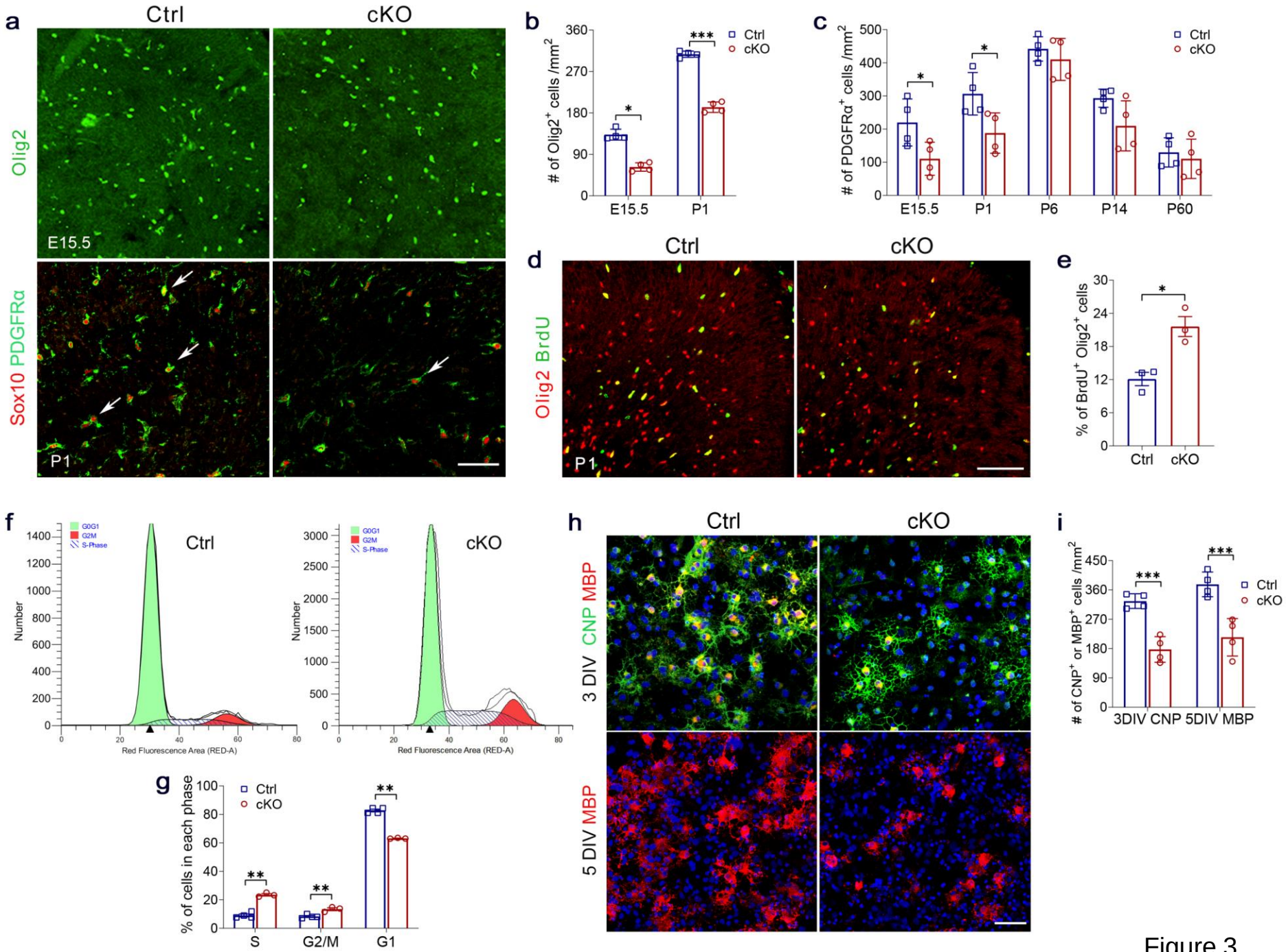
a
Ctrl
cKO
Olig2
E15.5
Sox10 PDGFRα
P1
b
# of Olig2+ cells /mm2
Ctrl
cKO
E15.5
P1
c
# of PDGFRα+ cells /mm2
E15.5
P1
P6
P14
P60
d
Olig2 BrdU
P1
e
% of BrdU+ Olig2+ cells
f
G0G1
G2M
S-Phase
Number
Red Fluorescence Area (RED-A)
g
% of cells in each phase
S
G2/M
G1
h
3 DIV CNP MBP
5 DIV MBP
i
# of CNP+ or MBP+ cells /mm2
3DIV CNP
5DIV MBP

Figure 3

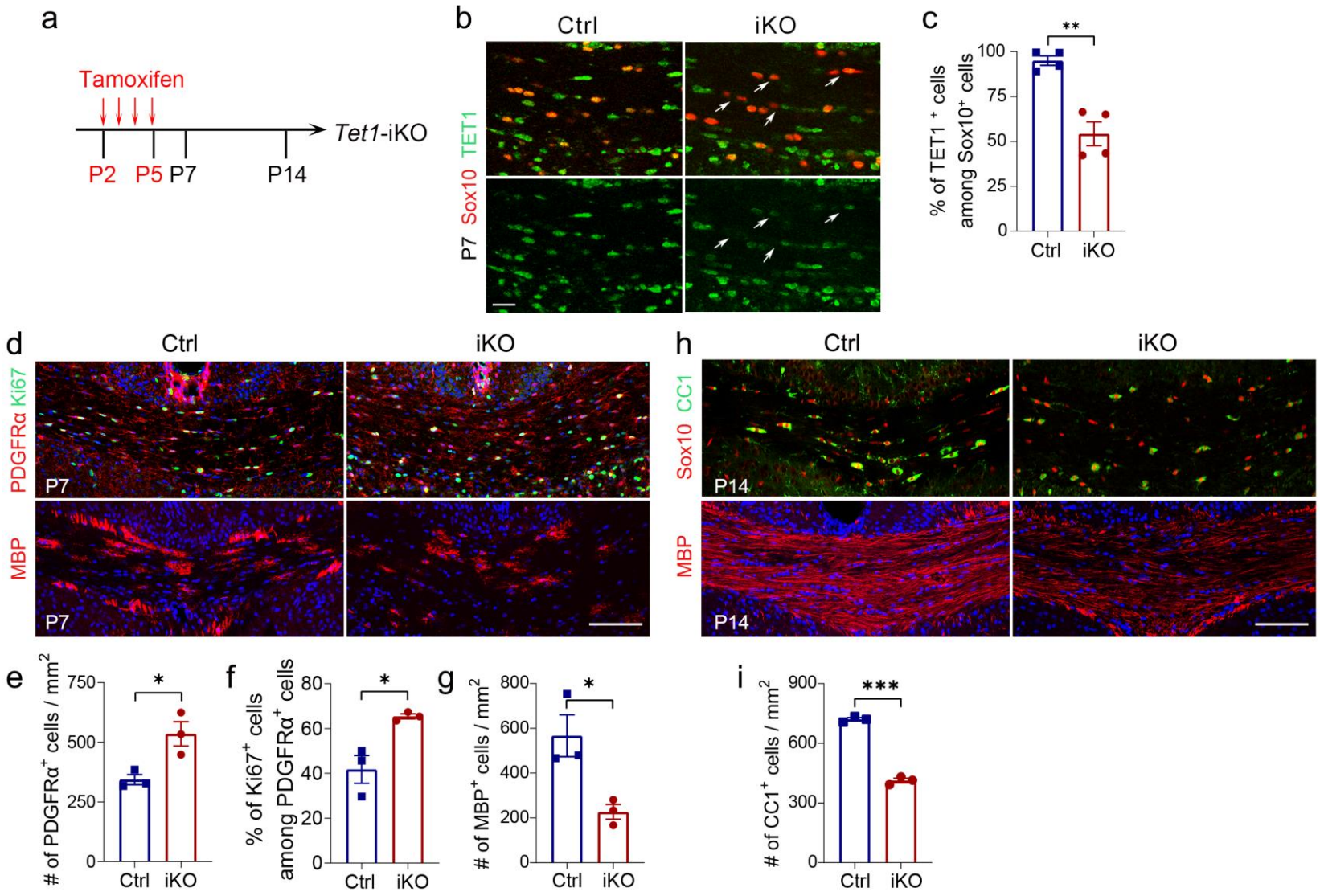
a
Tamoxifen
Tet1-iKO
P2
P5
P7
P14
b
Ctrl
iKO
TET1
Sox10
P7
c
**
% of TET1 + cells among Sox10+ cells
100
75
50
25
0
Ctrl
iKO
d
Ctrl
iKO
PDGFRα
Ki67
MBP
P7
P7
h
Ctrl
iKO
Sox10
CC1
MBP
P14
P14
e
*
# of PDGFRα+ cells / mm2
750
500
250
0
Ctrl
iKO
f
*
% of Ki67+ cells among PDGFRα+ cells
80
60
40
20
0
Ctrl
iKO
g
*
# of MBP+ cells / mm2
800
600
400
200
0
Ctrl
iKO
i
***
# of CC1+ cells / mm2
900
600
300
0
Ctrl
iKO

Figure 4

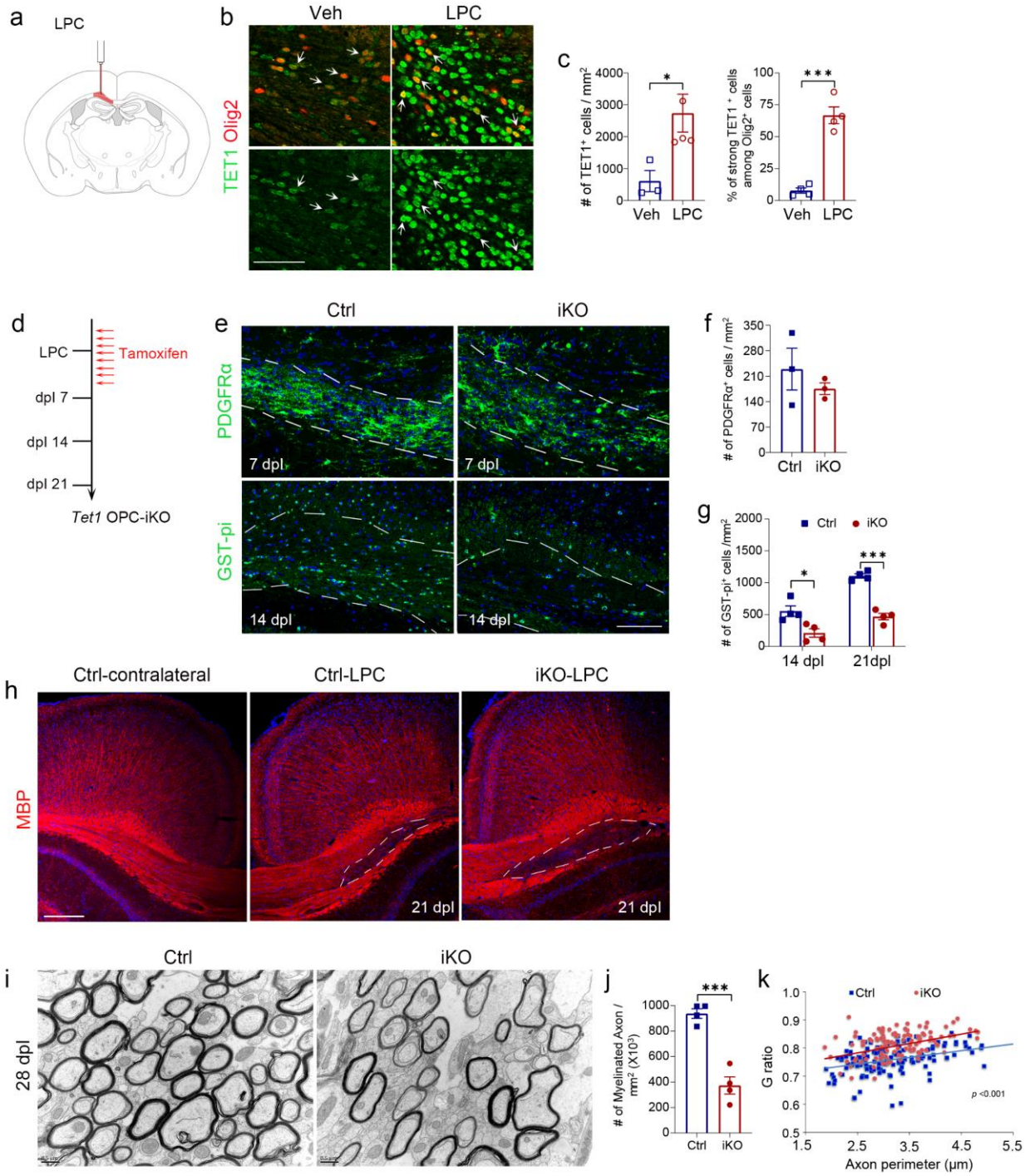
a
LPC
b
Veh
LPC
TET1 Olig2
c
# of TET1⁺ cells / mm²
Veh
LPC
% of strong TET1⁺ cells among Olig2⁺ cells
d
LPC
Tamoxifen
dpI 7
dpI 14
dpI 21
Tet1 OPC-iKO
e
Ctrl
iKO
PDGFRα
GST-pi
7 dpI
14 dpI
f
# of PDGFRα⁺ cells / mm²
Ctrl
iKO
g
# of GST-pi⁺ cells /mm²
14 dpI
21dpI
h
Ctrl-contralateral
Ctrl-LPC
iKO-LPC
MBP
21 dpI
i
Ctrl
iKO
28 dpI
j
# of Myelinated Axon / mm² (X10³)
k
G ratio
Axon perimeter (μm)
p <0.001

Figure 5

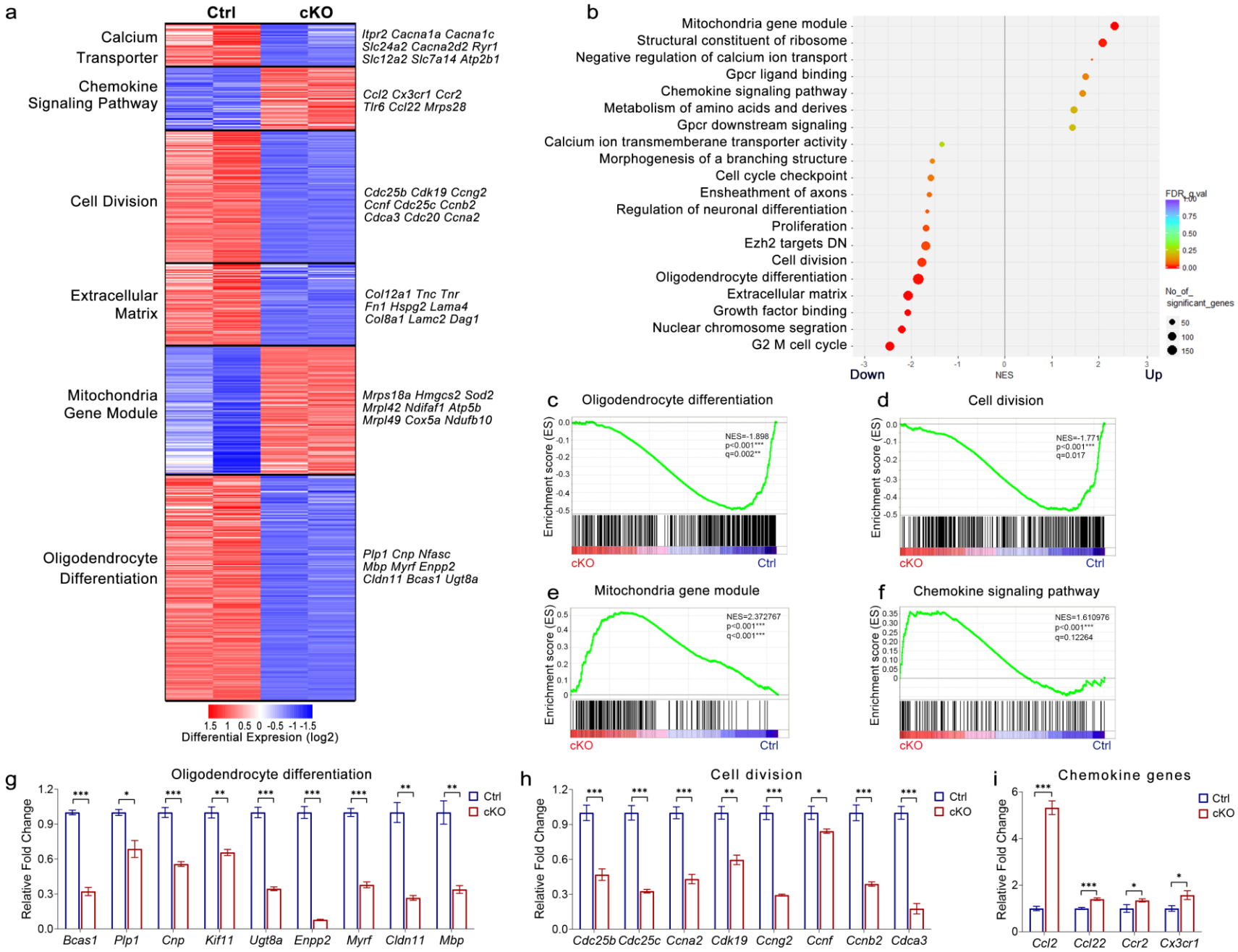
a
Ctrl
cKO
Calcium Transporter
Itpr2 Cacna1a Cacna1c Slc24a2 Cacna2d2 Ryr1 Slc12a2 Slc7a14 Atp2b1
Chemokine Signaling Pathway
Ccl2 Cx3cr1 Ccr2 Tlr6 Ccl22 Mrps28
Cell Division
Cdc25b Cdk19 Ccng2 Ccnf Cdc25c Ccnb2 Cdca3 Cdc20 Ccna2
Extracellular Matrix
Col12a1 Tnc Tnr Fn1 Hspg2 Lama4 Col8a1 Lamc2 Dag1
Mitochondria Gene Module
Mrps18a Hmgcs2 Sod2 Mrpl42 Ndifaf1 Atp5b Mrpl49 Cox5a Ndufb10
Oligodendrocyte Differentiation
Plp1 Cnp Nfasc Mbp Myrf Enpp2 Cldn11 Bcas1 Ugt8a
1.5 1 0.5 0 -0.5 -1 -1.5
Differential Expresion (log2)
b
Mitochondria gene module
Structural constituent of ribosome
Negative regulation of calcium ion transport
Gpcr ligand binding
Chemokine signaling pathway
Metabolism of amino acids and derives
Gpcr downstream signaling
Calcium ion transmemberane transporter activity
Morphogenesis of a branching structure
Cell cycle checkpoint
Ensheathment of axons
Regulation of neuronal differentiation
Proliferation
Ezh2 targets DN
Cell division
Oligodendrocyte differentiation
Extracellular matrix
Growth factor binding
Nuclear chromosome segration
G2 M cell cycle
Down
NES
Up
FDR_q_val
No_of_ significant_genes
c Oligodendrocyte differentiation
NES=-1.898
p<0.001***
q=0.002**
d Cell division
NES=-1.771
p<0.001***
q=0.017
e Mitochondria gene module
NES=2.372767
p<0.001***
q<0.001***
f Chemokine signaling pathway
NES=1.610976
p<0.001***
q=0.12264
Enrichment score (ES)
cKO
Ctrl
g Oligodendrocyte differentiation
Relative Fold Change
Ctrl
cKO
Bcas1 Plp1 Cnp Kif11 Ugt8a Enpp2 Myrf Cldn11 Mbp
h Cell division
Cdc25b Cdc25c Ccna2 Cdk19 Ccng2 Ccnf Ccnb2 Cdca3
i Chemokine genes
Ccl2 Ccl22 Ccr2 Cx3cr1

Figure 6

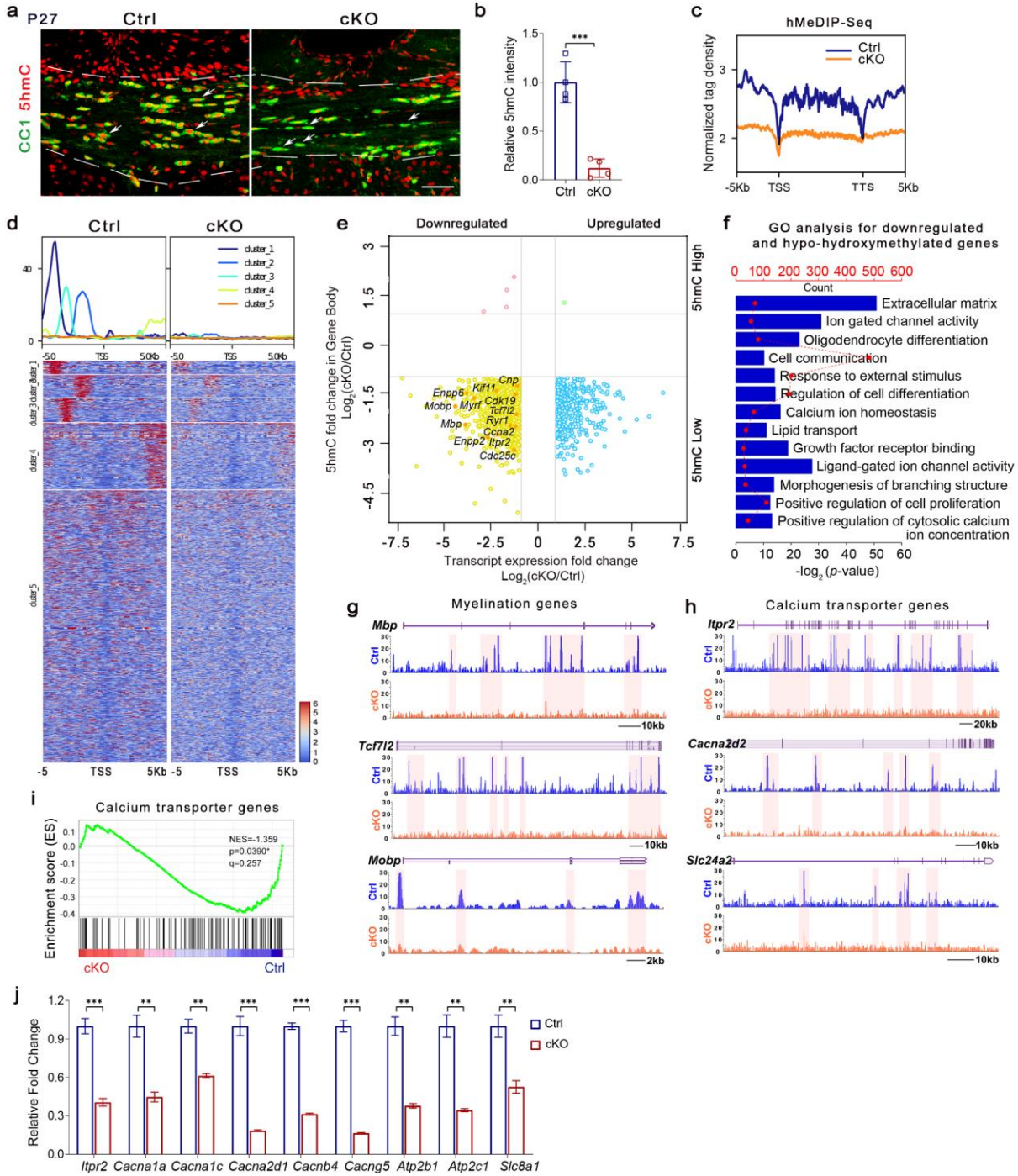
a
P27
Ctrl
cKO
CC1 5hmC
b
Relative 5hmC intensity
***
Ctrl
cKO
c
hMeDIP-Seq
Ctrl
cKO
Normalized tag density
-5Kb
TSS
TTS
5Kb
d
Ctrl
cKO
cluster_1
cluster_2
cluster_3
cluster_4
cluster_5
-5
TSS
5Kb
e
Downregulated
Upregulated
5hmC High
5hmC Low
5hmC fold change in Gene Body
Log2(cKO/Ctrl)
Transcript expression fold change
Log2(cKO/Ctrl)
Cnp
Klf11
Enpp6
Cdk19
Mobp
Myrf
Tcf7l2
Ryr1
Mbp
Ccna2
Enpp2
Itpr2
Cdc25c
f
GO analysis for downregulated and hypo-hydroxymethylated genes
Count
Extracellular matrix
Ion gated channel activity
Oligodendrocyte differentiation
Cell communication
Response to external stimulus
Regulation of cell differentiation
Calcium ion homeostasis
Lipid transport
Growth factor receptor binding
Ligand-gated ion channel activity
Morphogenesis of branching structure
Positive regulation of cell proliferation
Positive regulation of cytosolic calcium ion concentration
-log2 (p-value)
g
Myelination genes
Mbp
Tcf7l2
Mobp
Ctrl
cKO
10kb
2kb
h
Calcium transporter genes
Itpr2
Cacna2d2
Slc24a2
20kb
10kb
i
Calcium transporter genes
Enrichment score (ES)
NES=-1.359
p=0.0390*
q=0.257
cKO
Ctrl
j
Relative Fold Change
Ctrl
cKO
Itpr2
Cacna1a
Cacna1c
Cacna2d1
Cacnb4
Cacng5
Atp2b1
Atp2c1
Slc8a1

Figure 7

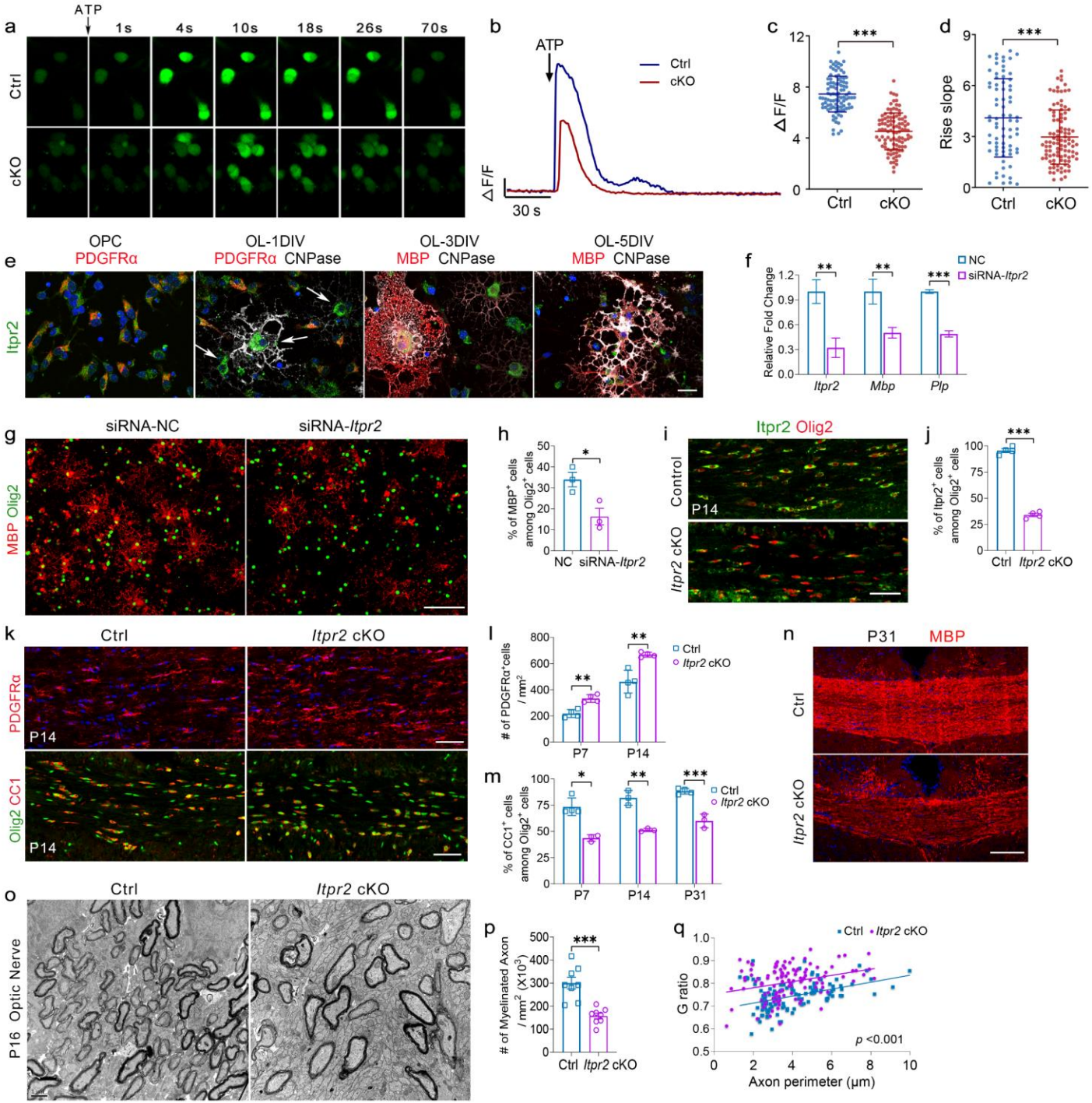
a
ATP
1s
4s
10s
18s
26s
70s
Ctrl
cKO
b
ATP
Ctrl
cKO
ΔF/F
30 s
c
***
ΔF/F
Ctrl
cKO
d
***
Rise slope
Ctrl
cKO
e
OPC
PDGFRα
OL-1DIV
PDGFRα CNPase
OL-3DIV
MBP CNPase
OL-5DIV
MBP CNPase
Itpr2
f
NC
siRNA-Itpr2
Relative Fold Change
Itpr2
Mbp
Plp
g
siRNA-NC
siRNA-Itpr2
MBP Olig2
h
% of MBP+ cells among Olig2+ cells
NC
siRNA-Itpr2
i
Itpr2 Olig2
Control
P14
Itpr2 cKO
j
% of Itpr2+ cells among Olig2+ cells
Ctrl
Itpr2 cKO
k
Ctrl
Itpr2 cKO
PDGFRα
P14
Olig2 CC1
P14
l
# of PDGFRα+cells / mm2
Ctrl
Itpr2 cKO
P7
P14
m
% of CC1+ cells among Olig2+ cells
Ctrl
Itpr2 cKO
P7
P14
P31
n
P31
MBP
Ctrl
Itpr2 cKO
o
Ctrl
Itpr2 cKO
P16 Optic Nerve
p
# of Myelinated Axon / mm2 (X10^3)
Ctrl
Itpr2 cKO
q
Ctrl
Itpr2 cKO
G ratio
p <0.001
Axon perimeter (μm)

Figure 8